Statistics and dynamics of the perturbed universe

Lemson, Gerard

Chapter 5

Density profiles from dissipationless collapse

1   Introduction

In recent years the study of structure formation in the Universe has entered a new regime through the inclusion of hydrodynamic processes. But even though much energy and CPU-time is spent on these dissipative processes, this does not imply that the gravitational, dissipationless aspects of this problem have been fully understood. Obtaining a good, if not complete, understanding of purely gravitational collapse is imperative for various reasons. First, gravity affects the formation of all structures, indeed in the most generally accepted theories of structure formation, it is the single most important agent in starting the collapse in the first place. Second, probably all structures have gone through a phase where gravity was dominant, even late in their evolution. The hydrodynamic processes then act within a background shaped by gravity (White & Rees, 1978). Third, some structures are believed to have been shaped by gravity alone. Most notable among these are elliptical galaxies and the dark halos that are believed to make up most of the mass of spiral galaxies.

A curious problem is that these two classes of objects appear to have very different shapes. It has been long appreciated that the $R^{1/4}$–profile, proposed by de Vaucouleurs (1948), gives a good fit to the surface brightness profiles of many elliptical galaxies (see also Schombert, 1986). Sarazin (1988) suggests that the $R^{1/4}$ profile also provides a good fit to the surface density distribution of galaxies in clusters, which is supported by West et al. (1987, 1989). The deprojected density profile (Young, 1976) corresponding to the $R^{1/4}$ profile is similar to the family of models investigated by Tremaine et al. (1993) and Dehnen (1993), defined by

$$\rho_\eta(r) = \frac{\eta}{4\pi} \frac{M_\eta R_\eta}{R_\eta^{3-\eta}(r + R_\eta)^{1+\eta}} \; . \tag{5.1}$$

The well known models by Jaffe (1983) and Hernquist (1990), which were proposed mainly because they bear such resemblance to the $R^{1/4}$–profile, are obtained for $\eta = 1$ and $\eta = 2$ respectively. On the other hand, the dark halos around spiral galaxies are usually modeled

using truncated isothermal spheres (e.g. van Albada et al., 1985):

$$\rho(r) = \frac{\rho_0}{1 + (r/a)^2} \; . \tag{5.2}$$

This model is used mainly because it explains the flat rotation curves of spiral galaxies, which naively imply an asymptotic density profile $\rho \sim r^{-2}$.

Both models have their particular theoretical explanation. Isothermal systems are thought to be the outcome of violent relaxation (Lynden-Bell, 1967), but the fact that violent relaxation is probably never complete has instead been used as an argument to explain the development of $R^{1/4}$ profiles (May & van Albada, 1984; Hjorth & Madsen, 1991). Indeed, N-body simulations have shown that cold and clumpy initial conditions, thought to be prerequisites for violent relaxation, evolve into objects with approximately $R^{1/4}$ surface density profiles (van Albada, 1982). More realistic initial conditions, where the initial structure of the proto-cluster was obtained using cosmologically reasonable fluctuation spectra, also evolve into objects with density profiles corresponding to the de Vaucouleurs form (Dubinski & Carlberg, 1991; Katz, 1991). A completely satisfying, analytical explanation of how violent relaxation leads to objects of this form has so far been lacking and the fact that these results were almost exclusively obtained from more or less isolated collapses has cast some doubt on the relevance of these calculations for objects evolving in cosmologically realistic environments (Zaroubi & Hoffman, 1993).

These problems seem to be absent in an alternative approach, which reproduces power-law density profiles such as those needed to explain flat rotation curves, using generalizations of the spherically symmetric top-hat model (Gunn & Gott, 1972). Originally intended to describe the density profiles of ellipticals, this semi-analytical approach, when combined with assumptions about the (power-law) cosmological initial conditions, is able to explain power-law density profiles, $\rho \sim r^{-\gamma}$, with γ dependent on the cosmological parameters (Fillmore & Goldreich, 1984; Bertschinger, 1985). These predictions are claimed to be corroborated by cosmological N-body simulations, using power-law initial fluctuation spectra (e.g. Quinn et al., 1986; Efstathiou et al., 1988; Crone et al., 1994). This would suggest that, indeed, violent relaxation is *not* the prime agent determining the shapes of the final relaxed objects. The main limitation of these cosmological simulations is that the resolution to which the resulting clusters can be probed is much lower than what can be reached in isolated collapse simulations. Consequently, the density profiles are much less well determined and unknown force softening effects may play a much greater role. Furthermore, the analytical results are based on purely radial infall and relaxation. One must doubt whether these calculations are still relevant during the violent collapse phases such as are observed in the N-body simulations.

It is unsatisfying that collapse processes governed by the same agent seem to give rise to very different outcomes. On the observational side one may claim that the mentioned objects are simply not shaped by gravitational collapse alone. This is probably true to some extent, but one must certainly also doubt that we understand purely gravitational collapse completely. Recently, some results have been obtained, both by observational and theoretical means, which suggest that a more unified view is possible. Sanders & Begeman (1994) have modeled galaxy rotation curves using the density profile suggested
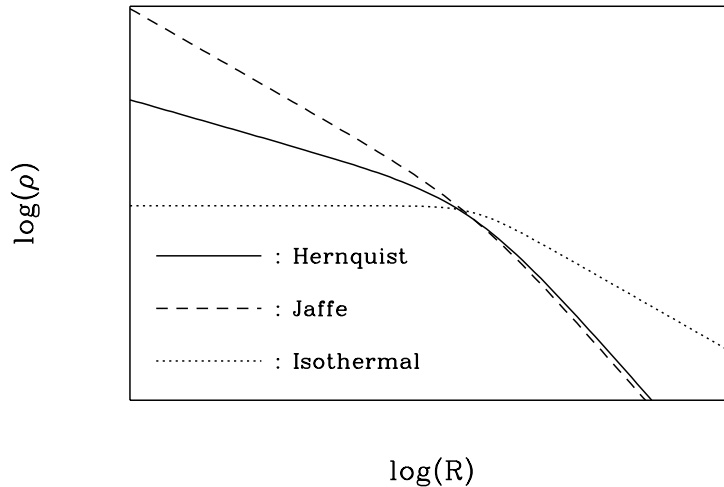
Figure 1: *Comparison of three models for the density profile. The Hernquist and Jaffe profiles are defined in Eq. 5.4, the truncated isothermal profile is defined in Eq. 5.2.*

by Hernquist (1990) for the dark halo . They obtained excellent fits for the rotation curves using this model, and moreover found a relation between the total mass of the halo and the characteristic scale of the halo model,

$$M \propto R^2 \quad . \tag{5.3}$$

This relation is equivalent to a relation found by Fish (1964) for elliptical galaxies and to the similar relation for Abell clusters as determined by West et al. (1989). Dubinski & Carlberg (1991) found that the Hernquist model also provides a very good description of the density profile of the CDM halos in their high resolution collapse simulations. Their simulation was not fully cosmological, but they approximated the effects of external structures by introducing a linearly evolving tidal field. In this way they were able to simulate the collapse of CDM clusters/halos with much higher resolution than would have been possible using fully cosmological simulations.

Finally, in chapter 4 of this thesis, it was shown that, whereas clusters in realistic simulations follow the simple top-hat model (Gott & Gunn, 1972; Chapter 4) until turn-around, the outcome of the virialization process differs from the predictions. In the generalization of the top-hat model to spherical density perturbations with a general power-law profile, it is often assumed that all radii recollapse to a fixed fraction of their turn-around radius (Gott & Rees, 1975; Hoffman & Shaham, 1985) and this assumption is confirmed by the semi-analytical calculations of Fillmore & Goldreich (1984) and Bertschinger (1985). However, in chapter 4 it was shown that larger radii collapse by smaller factors than inner ones, showing that these calculations do not correctly describe the relaxation process of clusters in cosmological simulations.

In this chapter we will investigate the density profiles of these simulated clusters in detail. We will do so by comparing these profiles to the Hernquist and Jaffe profiles respectively.

For completeness, these are defined by

$$\text{Hernquist} \quad : \quad \rho(R) = \frac{M_H R_H}{2\pi R(R + R_H)^3}$$

$$\text{Jaffe} \quad : \quad \rho(R) = \frac{M_J R_J}{4\pi R^2(R + R_J)^2} \ , \tag{5.4}$$

and they are drawn, together with the densiy profile for a truncated isothermal sphere, in Fig. 1. For this we need to determine accurate density profiles, since these models essentially only differ in the central regions. For instance how one chooses the center is of great importance. This will be discussed in the next section. We will fit the resulting profiles to the various models using non-linear two-parameter fits. We will also perform three-parameter fits to the models defined by (5.1), by adding η as a free parameter. Then the parameters obtained from the fits will be correlated and the results will be compared to observed correlations such as Fish's law. We will then investigate the density profiles resulting from isolated collapse simulations. Some of these, obtained from extracting proto-clusters from the cosmological simulations, were studied already in Chapter 4. Added to these are collapse simulations of initially spherically symmetric clusters with power-law density perturbation profiles, and clumpy collapses, similar to those studied by van Albada (1982). We will conclude with a summary and discussion.

2   Techniques

2.1   Methods for determining the density profiles

In Fig. 2 we plot two projections of a typical cluster extracted from one of the cosmological N-body simulations that are the main object of study of this chapter. These simulations were considered earlier in Chapter 4 and will be described below. Here we expose the problems for estimating radial density profiles of clusters and for fitting these profiles to the models, and we will present techniques to solve these. These problems originate from the fact that simulated clusters are in general not perfectly spherically symmetric structures. This deviation from exact spherical symmetry is most obvious through the occurrence of sub-structure, especially in the outer regions of the cluster, but also through the ellipsoidal shape of the main body. As argued in chapter 4, such deviations appear to have no significant effects on those aspects of the dynamical evolution that one expects for an object that *is* exactly spherical. These deviations do however cause problems for estimating the radial density profile.

The main problem lies in determining a physically meaningful definition of the cluster center around which to expand the density profile. The effects of incorrectly choosing the center can be seen from Fig. 3. There we show, for the cluster from Fig. 2, binned density profiles for various choices for the center, namely, the center of mass of the whole cluster, the median position of the individual cluster particles and the center of mass of respectively the 10% and 1% of the points with the lowest potential energy. Also shown is the profile around the point which, in projections along two orthogonal directions, has the highest surface density. For a correct treatment of the innermost radii, this choice is probably

Figure 2: two projections of a typical cluster from the n=-1 simulation. This cluster is used as an example in the rest of this Chapter for illustrating various technicalities connected to determining the density profile and fitting the results to the models.

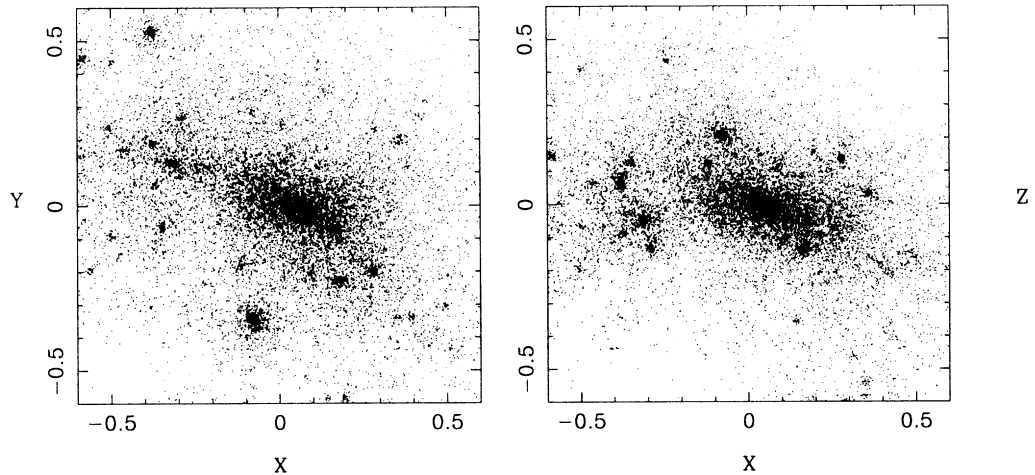around the point which, in projections along two orthogonal directions, has the highest surface density. For a correct treatment of the innermost radii, this choice is probably to be preferred. The center of mass of the whole cluster gives the worst estimate of the center, as is shown by the artificial flattening on small scales. This is because points at greater distances from the true center are weighted more heavily, and since deviations from sphericity are strongest there, this global center of mass is generally offset from the highest density peak. This causes the flattening of the profile at small radii, while in extreme cases the profile may even initially increase with radius. The smoothest results are obtained by taking the position of the highest density peak as center, while the center of mass of the 1% points with the lowest potential gives similar results. This last choice corresponds closely to the choice of Efstathiou et al. (1988), who use the position of the point with the lowest potential energy for the center of their clusters.

The differences between the various choices for the center suggest that the clusters have a dipole component in their mass distribution. A radial density profile obtained from a single, fixed center may therefore not give the best estimate of the mass distribution on all scales. To test the significance of this effect and to obtain a measure for this dipole moment we have applied the following technique. We iteratively determine the center of mass of spheres of decreasing size from the maximum radius inward. At the first step we take the center of mass of the whole cluster and around it draw a sphere of radius R_1 that must be large enough to contain all points of the cluster. At the next step we draw around the center of sphere 1 a sphere of a slightly smaller radius, $R_2 = R_1 - dR$, and calculate the center of mass of all points within this sphere. Around this center of mass, which will generally not coincide with the center of sphere R_1, we draw a sphere of *the same* radius R_2 and repeat the procedure until this center remains fixed. This is taken as the center on
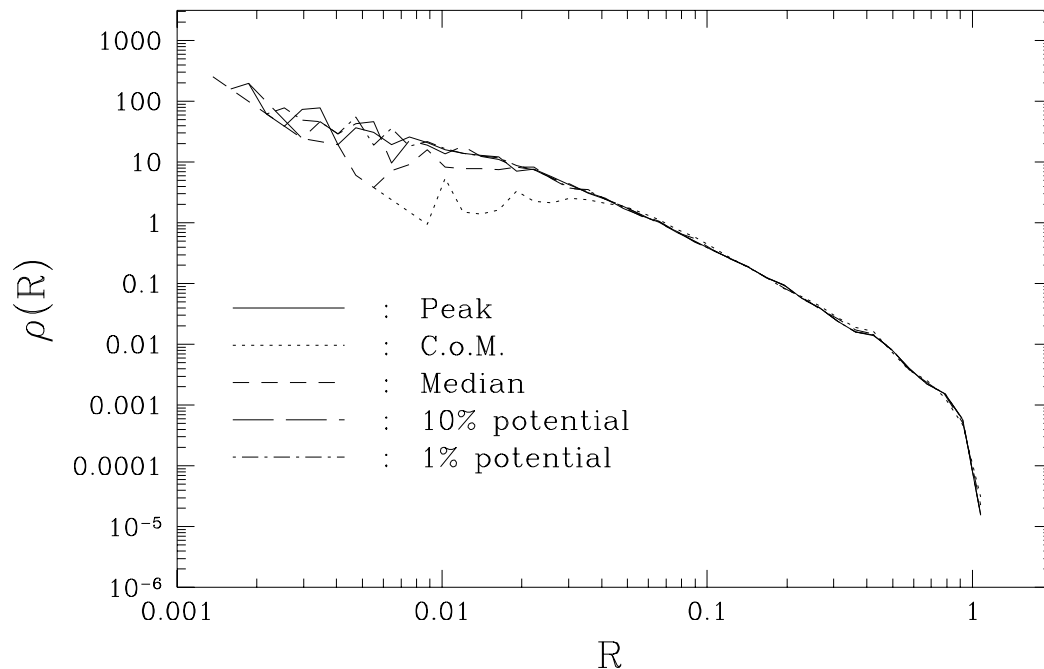
Figure 3: Density profiles for the cluster in Fig. 2, determined using various definitions of the center of the cluster: Peak indicates the peak of the surface density distribution. C.o.M. indicates the center of mass of the whole cluster. Median indicates the median of the coordinates of the points. 10% and 1% indicate the center chosen as the center of mass of the respective number of points with the lowest potential energy.

cumulative mass profile and quantitative information of the mismatch between the mass distributions on different scales, indicated by the positions of the respective centers.

In Fig. 4 we show for the cluster in Fig. 2 the walk that the center performs as function of scale. Also plotted are the various fixed centers used in determining the density profiles in Fig. 3. Ideally the last step should bring the center to the highest density peak and we see that this indeed is the case. In the same figure we show the spheres corresponding to the moving centers. This gives a nice illustration of the asymmetry in this cluster and shows that the center adjustment is not a smooth process but seems to occur in several steps causing a crowding of the circles at the corresponding radii. In Fig. 5 we show the cumulative mass profiles obtained using the moving center result as well as those obtained from the various fixed centers. The result from the moving center method is almost exactly equal to the result where the highest density peak is chosen for center. It shows that the precise positioning of the cluster center is most important for the inner regions.

It is interesting to speculate whether or not a dipole-mode of this kind, if also existent in dark halos around spiral galaxies, might be observed from the distribution and kinematics of the stars or HI-gas in those galaxies. There are many instances known where the gas
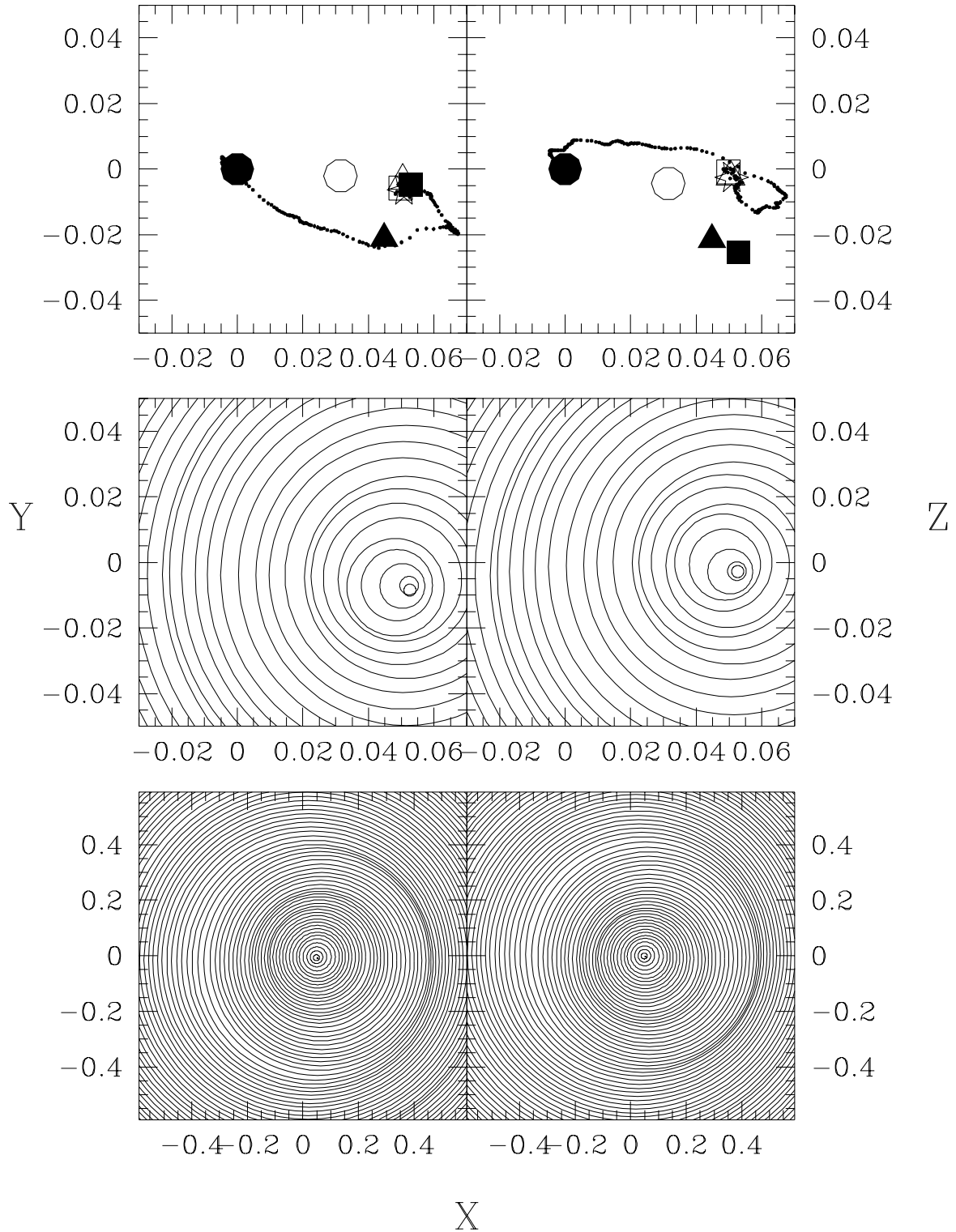
Figure 4: Determining the cluster center dependent on the sampling radius.
The upper diagram gives the cluster centers corresponding to the profiles in Fig. 3.
$\bigcirc$: C.o.M ; $\bullet$: median ; $\blacksquare$: 10% ; $\square$: 1% ; $\star$: peaks. The triangles correspond to
the centers determined by the maximum likelihood method, explained in § 2.2. $\triangle$ corre-
sponds to fits to the Jaffe profile, $\blacktriangle$ to fits to the Hernquist profile. The dots trace centers
according to the moving center approach as detailed in the text. The two lower frames show
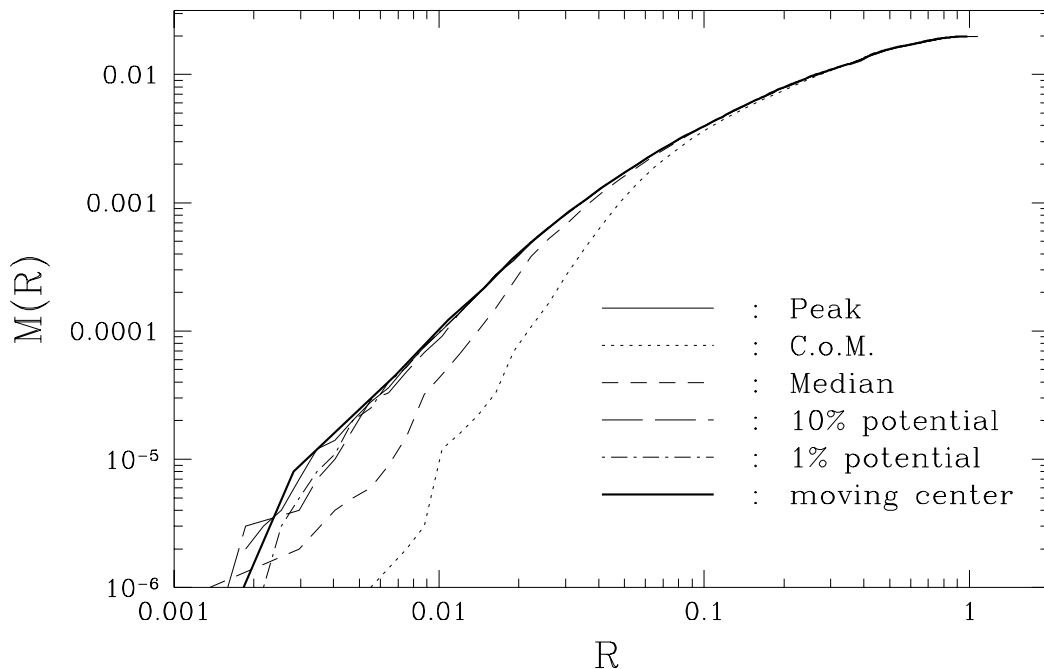*the corresponding spheres at two different scales.*

Figure 5: Same as Fig. 3, but now for mass profiles.

has a lopsided distribution (Baldwin et al., 1980; Richter & Sancisi, 1994; Rix & Zaritski, 1995) and there are hints that also the kinematic center is dependent on scale. In M101 for instance, the kinematic center seems to move with increasing radius in the direction of the asymmetric 'lobe' (Kamphuis, private communication).

Apart from this dipole mode, there are higher order distortions to the shape of the cluster which might influence the detailed shape of the density profile. The most important of these is the significant ellipsoidal quadrupole mode in most of the clusters. To determine the effect of this on the density profile, we show in Fig. 6 the density profile of the cluster in Fig. 2 as determined using ellipsoidal shells. The axial ratios and orientation of these shells were determined for one particular value, a, of the major axis. Starting with a sphere of radius a, we iteratively calculate the moment of inertia tensor of the particles inside it, and from this tensor determine the orientation and axial ratios of the corresponding ellipsoid. We then determine all the points inside this ellipsoid and iterate this process until the parameters do not change anymore. The density profile is then determined on concentric ellipsoidal shells with these axial ratios and orientation. In Fig. 6 this profile is plotted *not* versus the size of its semi-major axis a, but versus the quantity $r_{ell} \equiv (abc)^{1/3}$, where b and c are the sizes of the other two axes. This is the radius of the sphere that has the same volume as the ellipsoid with the given parameters. With this variable the ellipsoidal density profile agrees almost exactly with the radial density profile. We have therefore in this chapter concentrated exclusively on density profiles calculated using spherical shells.
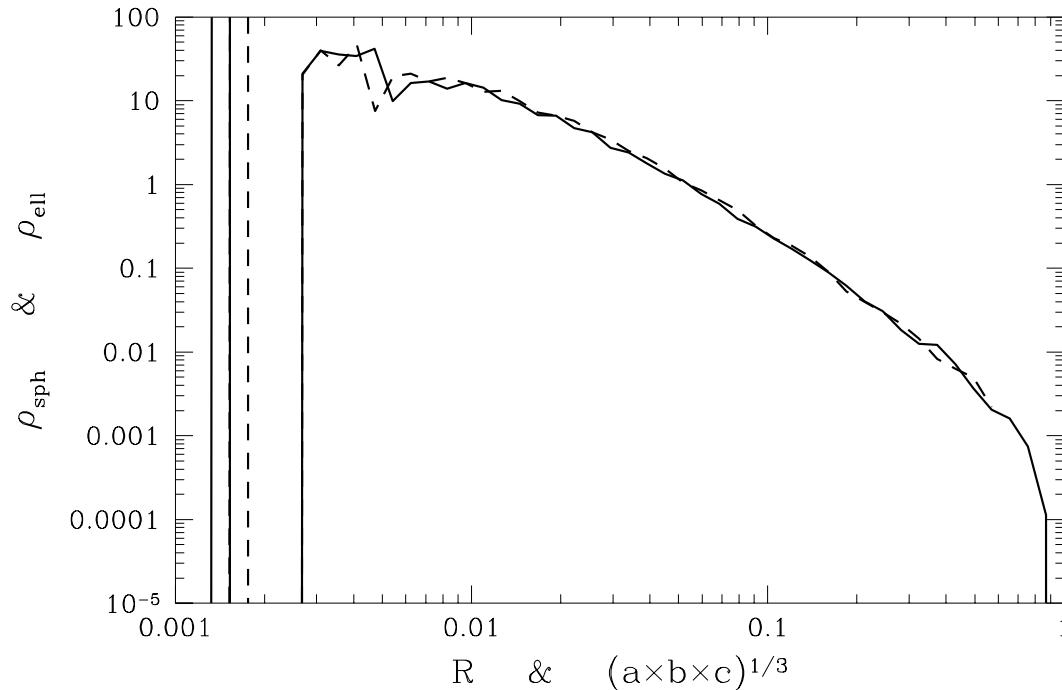
Figure 6: Density profiles for cluster in Fig. 2. The dashed line gives the density profile on ellipsoidal shells, with axial ratios determined by the method detailed in the text. The density is plotted versus the quantity $(abc)^{1/3}$, where a, b and c are the three semi-axes of the ellipsoid. The solid line is for spherical shells.

2.2   Fitting techniques

After determining the density profiles, we want to compare these to the class of models defined by (5.1), which has been proposed as a useful alternative to the $R^{1/4}$–model profile. The present analysis first concentrates on fitting the Hernquist and Jaffe models to the profiles (Hernquist, 1990; Jaffe, 1983). These models contain two parameters, the total mass M_c and a characteristic radius R_c, which determines the scale at which the model crosses from a $\rho \propto r^{\eta-3}$ to a $\rho \propto r^{-4}$ behaviour, where $\eta = 1, 2$ for the Jaffe and Hernquist models respectively. The choice which fitting method to use contains a number of subtleties, which will again be discussed with the cluster in Fig. 2 as example.

The standard fitting methods use χ^2-minimization, where

$$\chi^2 \equiv \sum_{i=1}^{N} w_i \big(\rho_{model}(r_i; \{\alpha_n\}) - \rho_{obs}(r_i)\big)^2 \tag{5.5}$$

where the α_n are the parameters and w_i are the weights which are generally taken to be $\sigma^{-2}(r_i)$. Minimization of this function with respect to its parameters gives by construction the minimum-variance solution (e.g. Eadie et al., 1971). However, instead of fitting to the density profile itself, one might also fit the model to the cumulative mass profile, or for instance to the rotational velocity profile v_{rot} as defined above. This last option would most closely agree with the determination of the density profiles of dark halos around

spiral galaxies (van Albada et al., 1985; Sanders & Begeman, 1994). In general the fitted parameters will be different for these different choices; in many cases, even just fitting the model to $\log(\rho)$ instead of to the ρ itself will already give different results. The cause of this can be understood from the maximum likelihood derivation of the χ^2–method. The standard assumption is that when the real model is given by $\rho_{ex}(r_i|M_c, R_c)$, the probability that one measures $\rho_{obs}(r_i) \pm \Delta_i$ is normally distributed

$$P(\rho_{obs}) = \frac{1}{\sqrt{2\pi\Delta_i^2}} \exp\left[-\frac{(\rho_{obs,i} - \rho_{ex,i})^2}{2\Delta_i^2}\right] \tag{5.6}$$

For N observations a log-likelihood function is defined by

$$
\begin{aligned}
\psi(\{r_i\}) &\equiv -2\log\left[\prod_{i=1}^{N} P(r_i|M_c, R_c)\right] \\
&= \sum_{i=1}^{N} \frac{(\rho_{obs,i} - \rho_{ex,i})^2}{\Delta_i^2} + \text{const}
\end{aligned}
\tag{5.7}
$$

which is to be minimized with respect to the parameters M_c and R_c. Clearly, when (5.6) gives the correct probability distribution for the value of ρ_{obs}, the distribution resulting from a non-trivial transformation $\mathcal{F}(\rho)$ will in general not be Gaussian, and while the least squares method will still give the minimum variance solution it will in general be biased.

Since we do not know the correct distribution we have fitted the models both to $\log(\rho)$ and to the cumulative mass profile, $M_{cum}(R) \equiv 4\pi \int_0^R r^2\rho(r)dr$. The profiles were determined both with the highest density peak as center and with the moving center method. The consistency of the different methods should give some indication of the bias involved in the fitting procedures.

Using the least-squares method we also must specify the weights for the individual data points. After fixing the center and the size of the bins there are no *observational* uncertainties left. For the simulations studied here, the data points may be viewed as a sampling of the true density field, and one expects noise to be introduced by this. In particular, one expects small bins to show greater scatter than larger bins, and we would like to give less weight to their contribution. We have therefore assumed Poisson weights, i.e. we have used the counts in the logarithmic bins as weight: $w_i = N_i$.

In general, working with unbinned data is preferable to using binned data, since in the process of binning one only uses part of the information available. We have therefore developed yet another method for fitting the models to the cluster data. This method is similar to that developed by Sarazin (1980) for fitting models to the angular distribution of galaxies in clusters on the sky, but differs from it in certain important aspects. Both Sarazin's and our methods use the positions of all the individual galaxies in the clusters to fit the position of the center together with the other model parameters, via a maximum-likelihood technique. For a certain choice of center, $\mathbf{x}_c$, and model parameters, in our case M_c and R_c, Sarazin defines the likelihood function

$$L_{Sar} \equiv \prod_{i1}^{N} \rho_{mod}(|\mathbf{x}_i - \mathbf{x}_c| \,|M_c, R_c) \quad, \tag{5.8}$$

where ρ_{mod} is the model. This function is to be maximized with respect to all the parameters, including $\mathbf{x}_c$. As Sarazin notes, increasing M_c will always increase L_{Sar} and he therefore fixes the total mass. For this reason we have chosen a different form for the likelihood function, that will allow us to vary the mass in the fitting procedure as well. Our choice is based on the cumulative mass profile instead of on the radial density profile. There is no simple, natural form for the corresponding probability distribution and we therefore make the ansatz that the probability that one finds M points within a sphere of radius R around the center has a normal form. The likelihood function is then defined by

$$L(\mathbf{x}_c, M_c, R_c) = \prod_{i=1}^{N} \frac{1}{\sqrt{2\pi\sigma^2(R_i)}} \exp\left[-(M_{cum}(R_i) - M_{model}(R_i))^2/2\sigma^2(R_i)\right] \qquad (5.9)$$

where $R_i = |\mathbf{x}_i - \mathbf{x}_c|$. Maximizing this function is equivalent to minimizing the log-likelihood function

$$
\begin{aligned}
\psi &\equiv -2\log(L) \\
&= \sum_{i=1}^{N} \left(\frac{(i \times m_p - M_{model}(R_i))^2}{\sigma^2(R_i)} + \log(2\pi\sigma^2(R_i)) \right)
\end{aligned}
\qquad (5.10)
$$

where m_p is the mass per particle and the points are ordered such that the individual R_i are increasing with i. For the results presented below we have assumed the Poisson form for the variance $\sigma^2(R_i) \equiv m_p M_{model}(R_i)$. Using the algorithm AMOEBA from Press et al. (1989) we minimize this function for the Jaffe and Hernquist models. For the cluster in Fig. 2 the centers that are found using this method are plotted as the open and filled triangles in Fig. 4. The center as determined from the fit to the Jaffe model is closer to the highest density peak than the one obtained from the Hernquist fit. This is probably due to the fact that the Jaffe profile is steeper in the inner regions, $\rho_J \propto r^{-2}$ and the method will search for the steepest density drop which will be associated with the local density maximum. The Hernquist model is flatter in the inner regions, $\rho \propto r^{-1}$, and may actually fit better with the center somewhat displaced from the density maximum, as happens to be the case for this cluster.

3   Results I: cosmological N-body simulations

3.1   Results from the cosmological simulations

Our investigations have concentrated on the study of two large cosmological N-body simulations that were provided by Simon White. These have been described elsewhere (Chapter 4; see also White, 1993), and here we will review the most important aspects. Both simulations contain 10^6 particles that were distributed uniformly throughout the simulation cube, but for density perturbations which followed a Gaussian random field with a power-law power spectrum, $P(k) \propto k^n$, with $n = -1, 0$. These were evolved in time with a particle-particle particle-mesh (PPPM) algorithm, where the PM-part used a grid of 256^3 cells and the PP-part had a force-softening parameter, ϵ, of size $\epsilon = L/2500$, with L the size of the
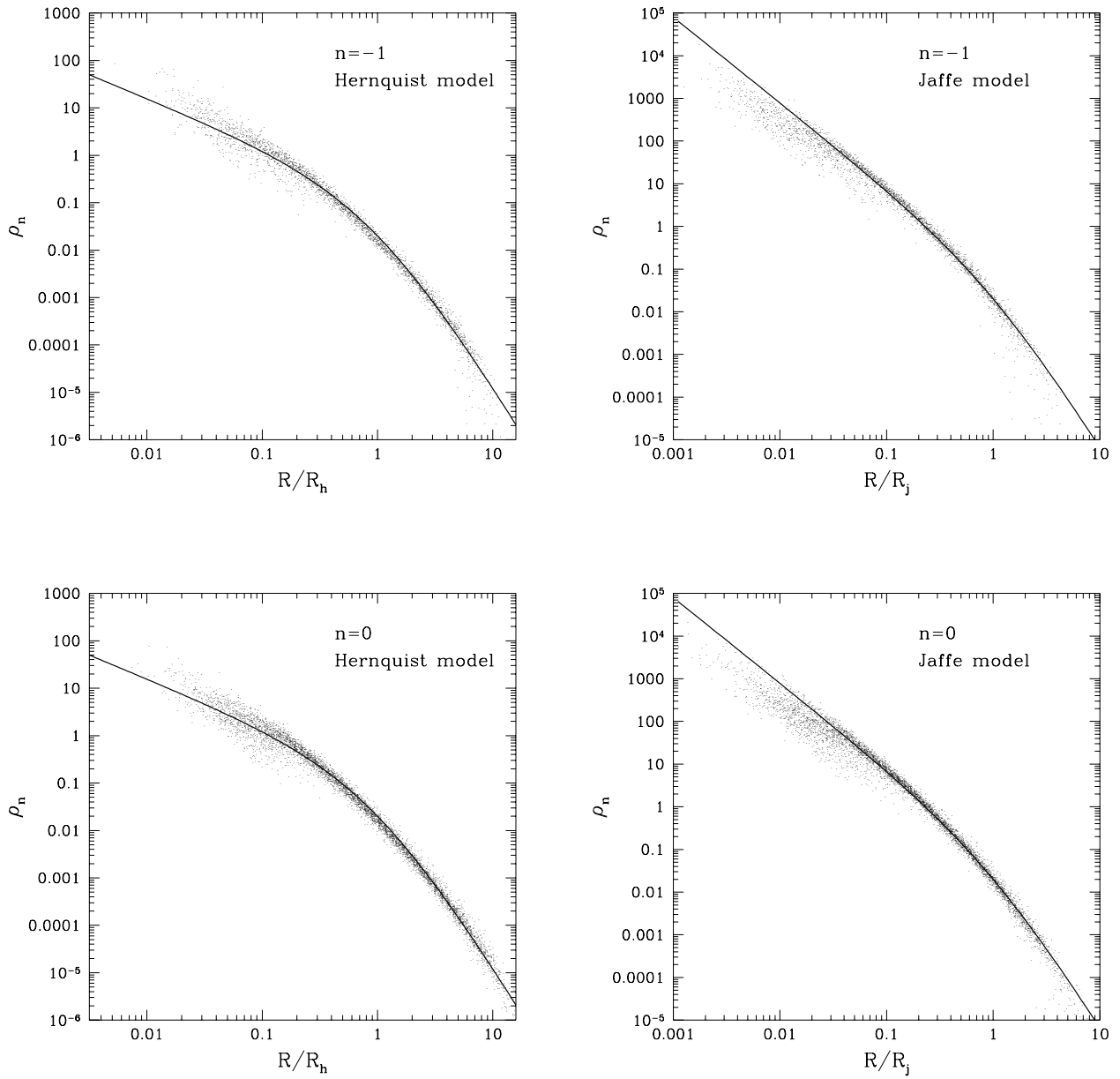
Figure 7: Density profiles for massive clusters in n=−1 (upper frames) and n=0 (lower frames) simulations, normalized using parameters from fits to Hernquist (left) and Jaffe (right) model.
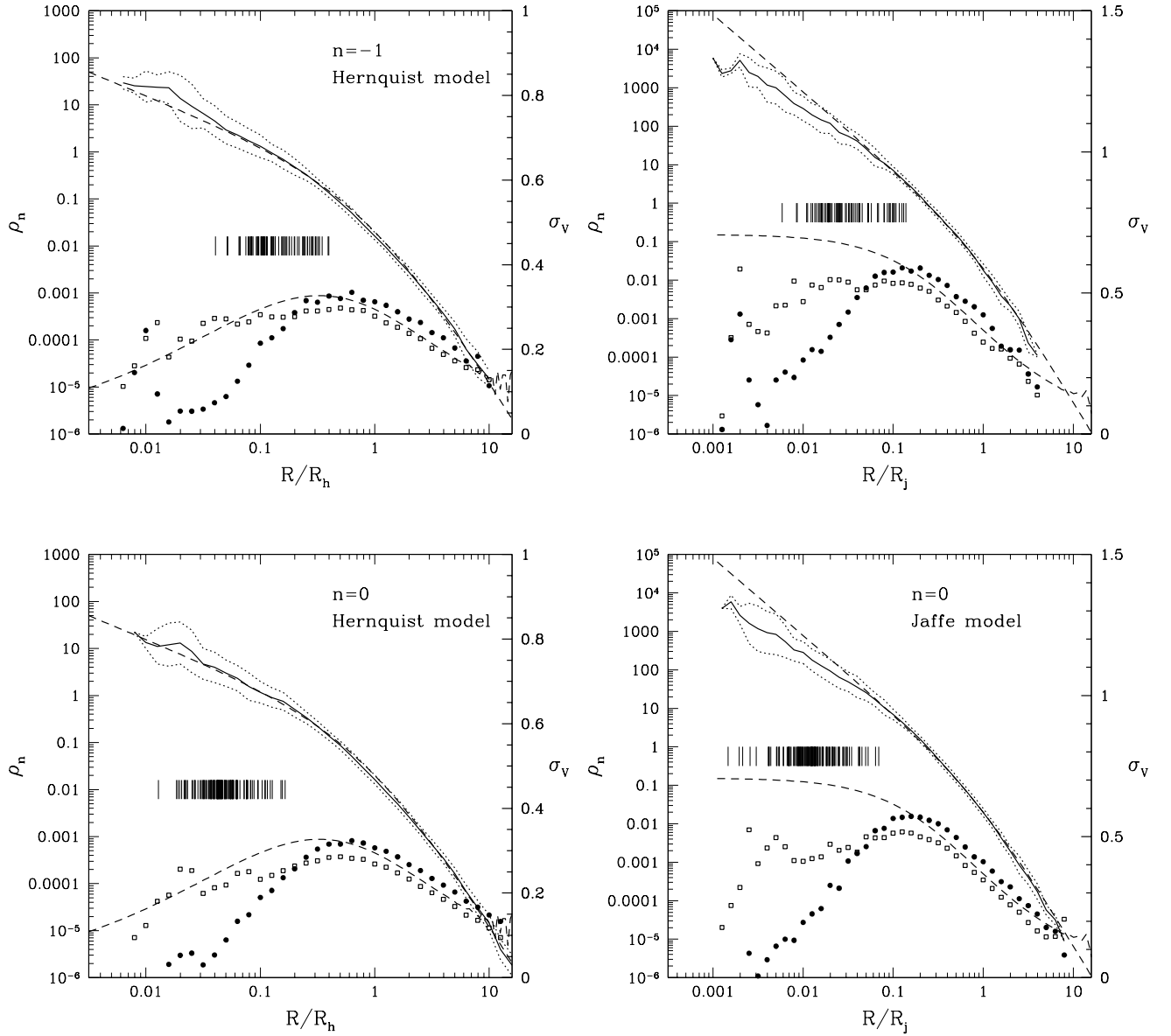
Figure 8: Density profiles from Fig. 7 averaged over all clusters, dotted lines give uncertainty in the average. The upper dashed lines give Hernquist model (left) and Jaffe model (right). Bar-codes show the correspondingly renormalized values of the force-softening radius. Also plotted are the tangential and radial velocity dispersions, respectively open squares and filled dots. The lower dashed lines give the model predictions for an isotropic velocity distribution.

simulation cube (for details of the algorithm see Hockney & Eastwood, 1981; Efstathiou et al. 1985). The clusters under consideration here were extracted from the last output time of the simulations using a standard friends-of-friends (fof) algorithm (e.g. Efstathiou et al. 1985). With a linking length that was 10% of the mean inter-particle spacing, we determined the centers-of-mass of the most massive clusters. Around these centers we determined the spheres within which the overdensity with respect to the whole simulated volume was $\delta_c = 50$, and we took all the points contained in these spheres to form the final clusters. Note that this is a lower value for the overdensity than the $\delta_c = 200$ used in Chapter 4, and the clusters will consequently be somewhat larger. We used all the clusters which had an 'fof-core' containing at least 1000 particles, which yielded 60 clusters for the n=−1 simulation and 111 clusters for the $n = 0$ simulation. To these we added about 25 clusters, whose fof-cores contained between 200 and 1000 particles, and were roughly uniformly chosen from this range.

For these clusters we determined density and mass profiles around the position of the highest density peak, and mass profiles using the moving center method. We fitted Hernquist and Jaffe models to these profiles using a standard non-linear least-squares routine. The results from the density profile fits are shown in Fig. 7. In this figure we show all the individual density profiles after normalizing them using the fitted parameters. In Fig. 8 the individual profiles are averaged and compared to the models. Clearly, the Hernquist profile gives an excellent fit to the average cluster profile over the whole range of radii *and* for both the n=−1 and n=0 simulations, although it may be somewhat low in the central parts. The Jaffe profile is equally well able to fit the model in the outer parts, but is too steep in the inner parts. The 'bar-codes' in Fig. 8 show the distribution of renormalized force-softening radii. The main discrepancy between the models and the mean profiles appears at radii smaller than the softening radius. Crone et al. (1994) correct their density profiles for this force softening. They use an argument based on an adiabatic invariant of the particle orbits under the change of zero to finite softening. This should steepen the profiles and the Jaffe model might then actually provide the better fit. On the other hand, in the inner parts discreteness effects will probably destroy the correspondence of the simulation to dark halos or clusters in the Universe anyway, and we have therefore chosen to present the results without this correction.

Fig. 8 also shows the average velocity dispersion profiles, both for the radial and the tangential components. The lines drawn through these points give the isotropic solutions for a spherical model cluster, as derived for instance in Tremaine et al. (1993). Although the velocity dispersion is not isotropic for all radii, the model curves fit the results reasonably well, with again a discrepancy in the inner regions for the Jaffe model.

Due to the unknown effects of the finite softening radius of the force calculation, no compelling case can be made for either of these two models as providing the best description of the 'data'. We have therefore also performed three-parameter fits to the density profiles using the more general class of η-models (Tremaine et al., 1993) as defined in Eq. 5.1. In Fig. 9 we show the distribution of the fitted values for η for all the clusters in the two simulations. The values of η are comparable for the two simulations and lie roughly between 1 and 2, the values for the Jaffe and Hernquist models. The average values of η for the two simulations are similar: $< \eta > \sim 1.6$. There is no trend of η with mass, but there is a trend

of η versus R_η, such that high values of η imply low values of R_η. R_η measures the radius at which the logarithmic slope of the profile reaches the value $(\eta - 7)/2$ and is thus clearly coupled to η. This shows that the scale parameter R_η itself is not well suited to use for a measure of the characteristic scale of the cluster. Below we will show that a combination of R_η and η does provide a good characterization of the size of the clusters.

In Fig. 10 we compare the parameters obtained from the different profile definitions and fitting methods to each other. It shows that in general the methods agree quite well although there are exceptions for individual clusters. The clusters which show the greatest
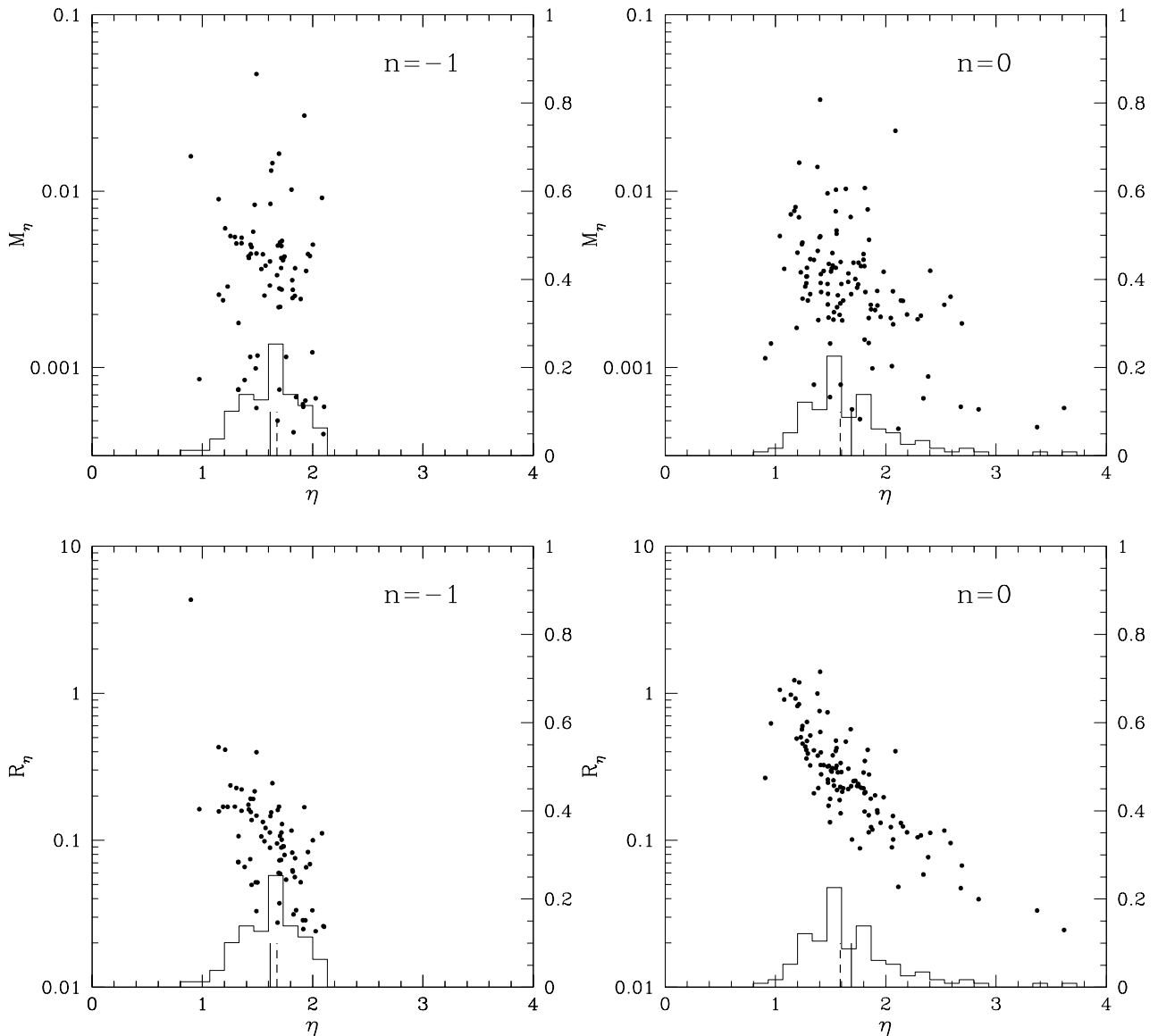

Figure 9: Correlations of parameters from three-parameter fits. M_η and R_η vs η. Left for clusters from n=−1 simulation, right for n=0.
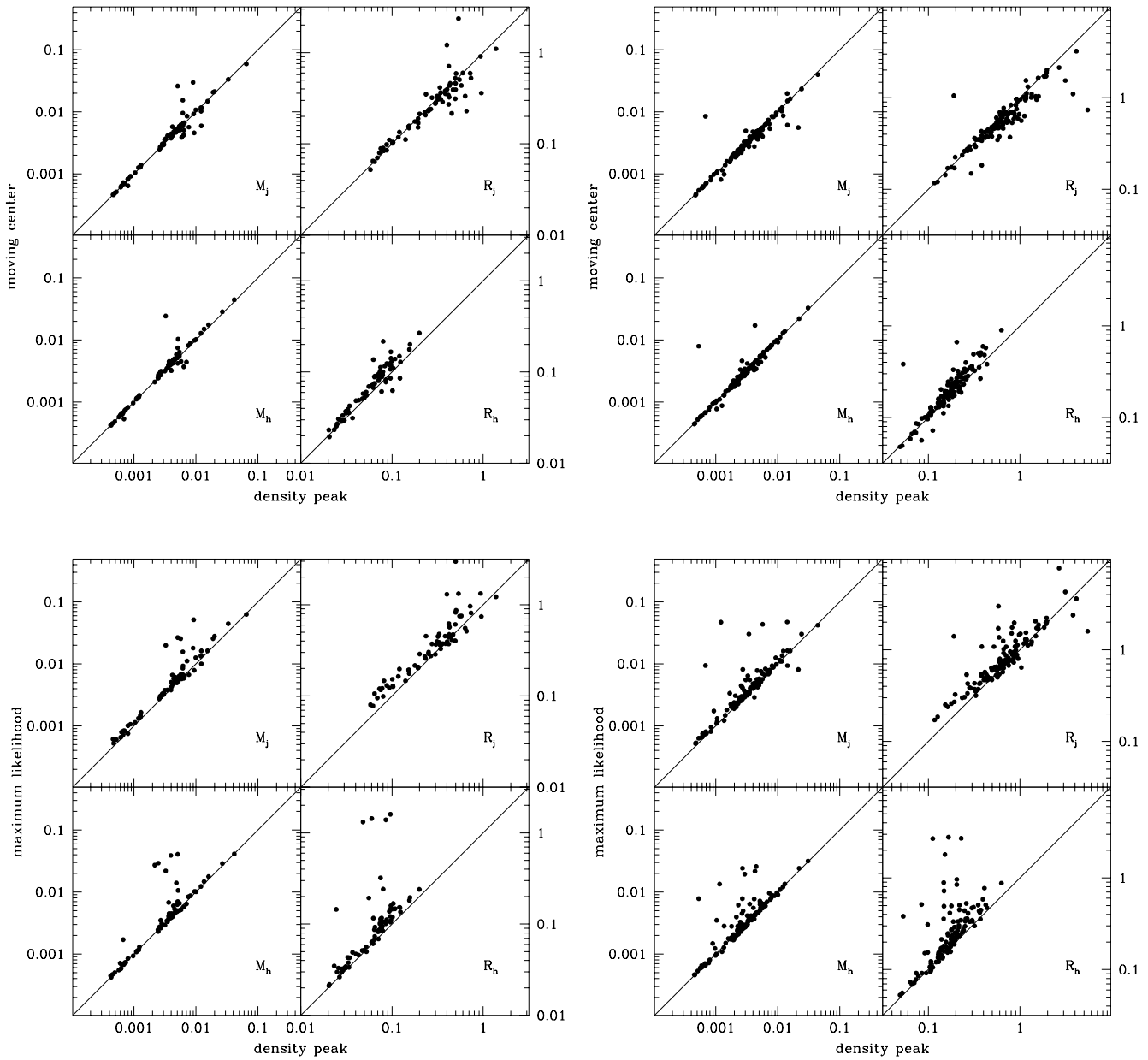
Figure 10: Comparison of fitted parameters for different methods for defining the density profiles. Plotted are parameters from fits using moving-center method versus density profiles around highest density peak (upper panels), and maximum-likelihood fits versus the highest density peak (lower panels). Indicated in the panels are the parameters which are compared. Again, the left panels show the results for the n=−1 simulation, right for n=0.

discrepancies, generally also show significant deviations from spherical symmetry, both in the core and in the outer regions.

Another interesting relation is the one between the centers found by the moving center
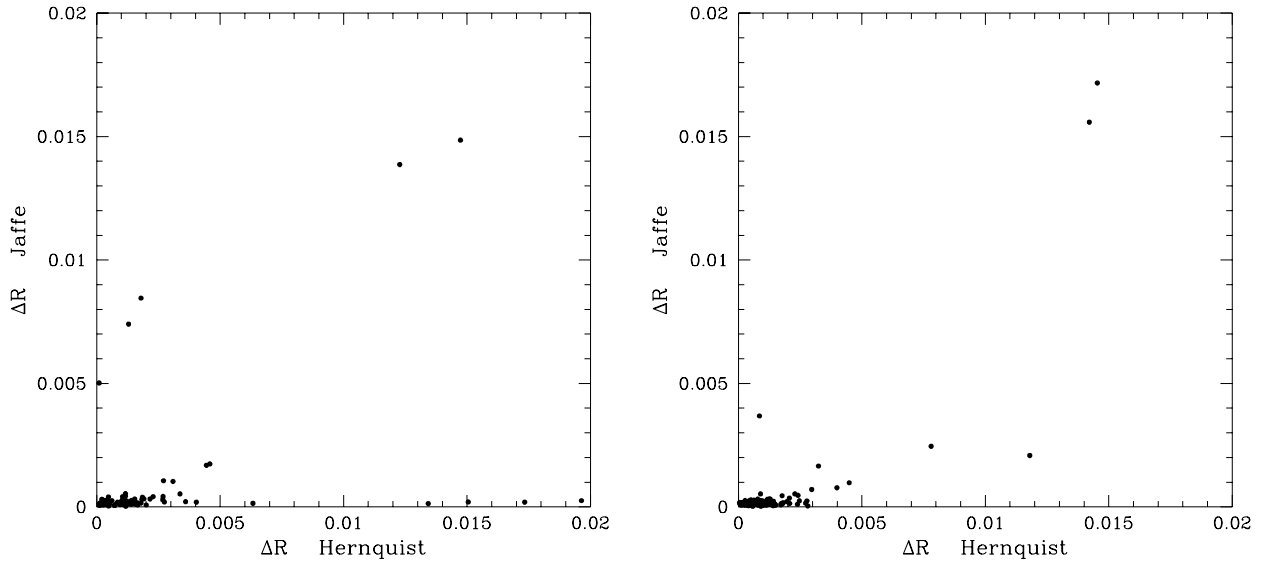
Figure 11: Comparison of the centers found with two different algorithms.

method at the smallest radius and the centers found by the maximum likelihood method. As Fig. 11 shows, the maximum likelihood fit to the Jaffe model finds the highest density peak with greater accuracy than the fit to the Hernquist model. But as Fig. 10 shows, the model parameters that are found, generally agree very well also for the Hernquist fits.

3.2 $R \propto M^{\beta}$

In Fig. 12 we show the model parameters obtained from the fits to the highest peak density profiles. Clearly the two parameters are strongly correlated. A fit to a power law relation, $R_c \propto M_c^{\beta}$ gives

$$n = -1 \quad : \quad R_H \propto M_H^{0.49 \pm 0.04}$$
$$R_j \propto M_J^{0.66 \pm 0.06} \tag{5.11}$$
$$n = 0 \quad : \quad R_H \propto M_H^{0.57 \pm 0.04}$$
$$R_J \propto M_J^{0.77 \pm 0.06} \tag{5.12}$$

One notes that the relations depend on the model that is used for fitting. The relations for the Hernquist fits agree very nicely with similar relations obtained by Fish (1964) and Kaastra & van Bueren (1981) for elliptical galaxies, West et al. (1989) for clusters of galaxies and Sanders & Begeman (1994) for dark halos. West et al. give a prediction for the expected relation for clusters from power-law power spectra, $P(k) \propto k^n$:

$$R_c \propto M_c^{\beta}, \quad \beta = \frac{5 + n}{9 + n} \tag{5.13}$$

which gives $\beta = 0.5, 0.56$ for $n = -1, 0$ respectively. This prediction agrees perfectly with the relations for the Hernquist models. West et al. do not give a derivation of this relation
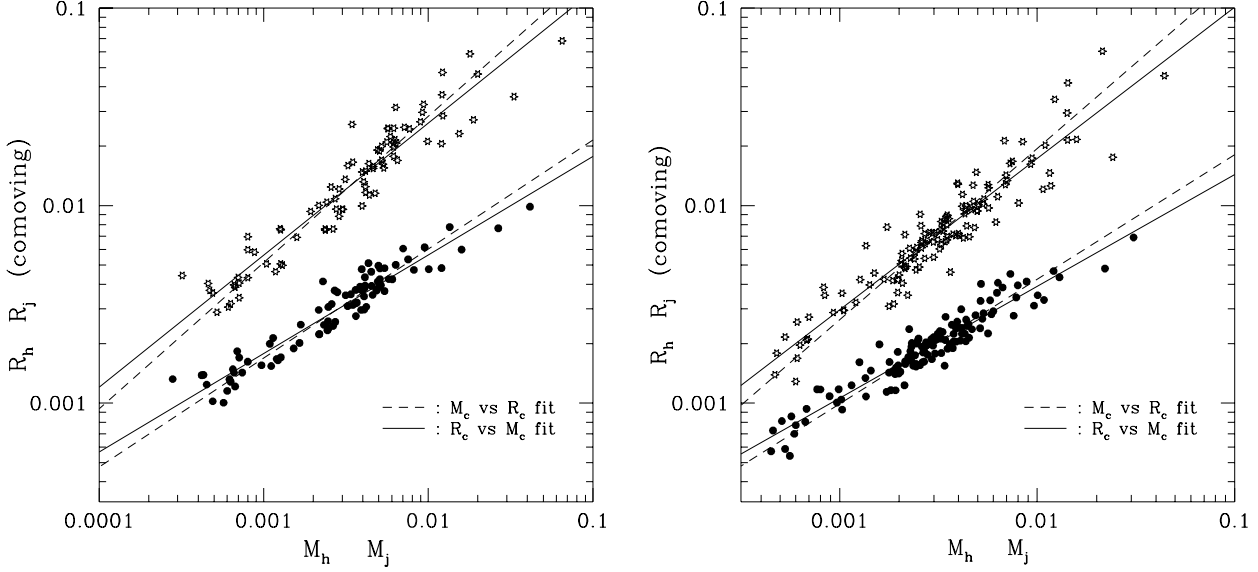
Figure 12: Correlations of parameters from two-parameter fits, for Hernquist and Jaffe model. The lines correspond to the fits in eqs. (5.11) and (5.12)

and it is different from that more often used in the literature (Chapter 4)

$$R_c \propto M_c^\alpha, \quad \alpha = \frac{5+n}{6} \tag{5.14}$$

This relation is closer to the fits to the Jaffe model, but disagrees with the Hernquist results.

The relations found by Fish and Kaastra & van Bueren were determined for quantities directly obtained from the data, i.e. without fitting models. In Fig. 13 we show similar results for the present simulations. There we show the specific total and kinetic energies versus the total mass. The potential energy is obtained from the isolated clusters with a particle-particle algorithm (e.g. Hockney & Eastwood, 1981). For the mass we simply take the total number of particles in the cluster multiplied by the individual particle's mass. Clearly these quantities are only rough approximations to the exact values; the effects on the energy from exterior structures is not taken into account, while the mass may be overestimated due to the inclusion of all particles within a density contour $\delta = 50$, while a more natural choice might be 200. Nevertheless, all these model-independent quantities show strong correlations, which are closer to the results from the Hernquist fits than to those from the Jaffe fits.

In Fig. 14 the correlation between the quantities M_η and R_η, obtained from the three-parameter fits to the η-models, are shown. This correlation has significantly greater scatter than the ones obtained with η fixed. However, when we plot the half-mass radius $R_{1/2} \equiv R_\eta/(2^{1/\eta} - 1)$ instead of R_η, the correlation is tighter again and, moreover, is very similar to the relations found before for the fit to the peak-density profiles. The reduction of the scatter is caused by the clear correlation between the value of η and the corresponding scale
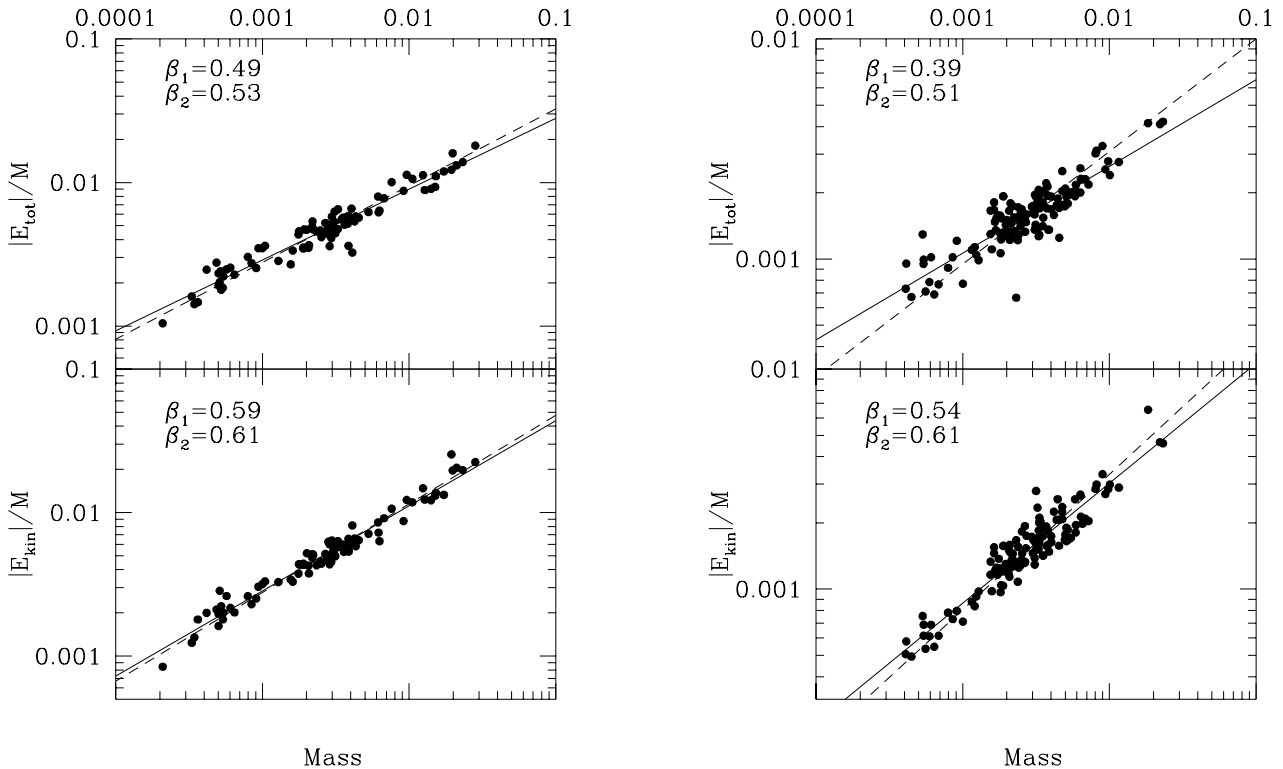
Figure 13: *Characteristic total energy and kinetic energy versus the total mass of the clusters in the cosmological simulations. These quantities are determined directly from the clusters, independent of model fits. The parameters β_i give the slopes of the fitted lines: β_1 is obtained from fitting the model $E/M \propto M^{\beta_1}$, β_2 is obtained from fitting the model $M \propto (E/M)^{1/\beta_2}$.*

factor R_η. This nicely illustrates a point made by Kormendy (1982) about the use of extra free parameters in fits. His main point is that when the main characteristics of an observed profile are already well described by a functional form with say two parameters, adding a third will in general not just serve to describe the remaining characteristics; it will more generally mix with one or both of the original parameters and so spoil the interpretation of these in terms of the physically relevant structural characteristics. In the case at hand, R_η not only determines the scale, but also the form of the profile and the same so for η. It is only a combination of the two that gives information on the spatial size of the clusters.

3.3 Rotation curves

For comparing the clusters in the simulations to the dark halos around spiral galaxies, it is useful to plot fiducial rotation curves, which are defined by

$$v_{rot}(R) \equiv \sqrt{\frac{GM(R)}{R}} \ . \tag{5.15}$$

In Fig. 15 we have plotted this quantity for all clusters individually, normalizing the size of the simulation cube of the last output frame to unity. From plots like these various authors
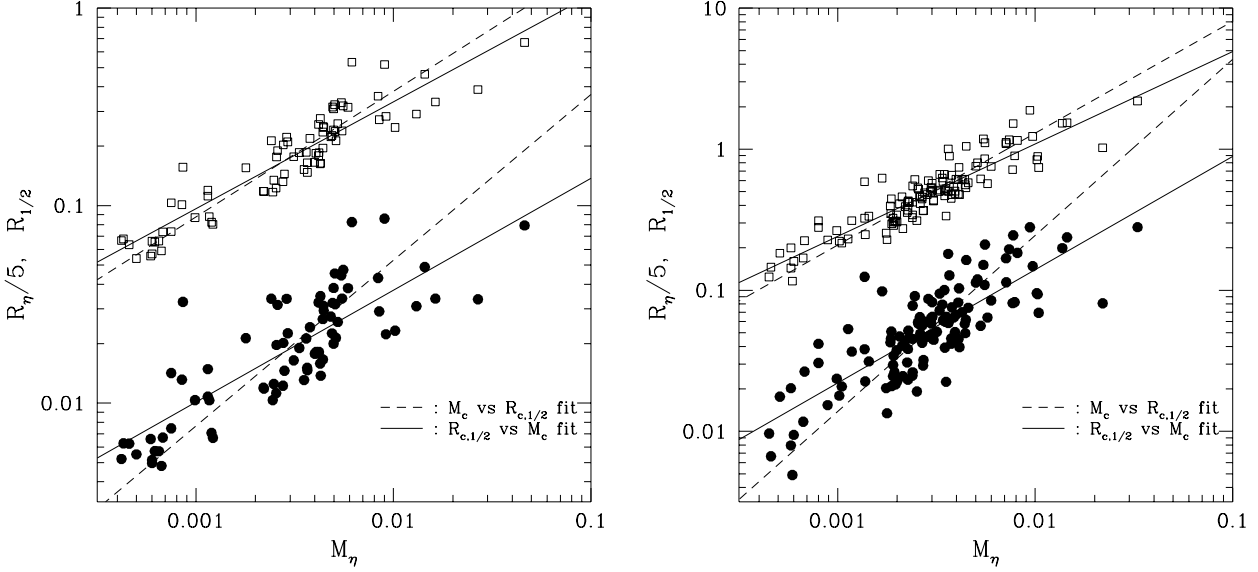
Figure 14: Correlation of R_η and corresponding $R_{50\%}$ with M_η. Due to correlation of η with R_η (see Fig. 9), correlation of $R_{50\%}$ with mass is tighter. Fitting $R_{50\%} \propto M_\eta^\beta$ gives $\beta = 0.54 \pm 0.02$ (n=−1) and $\beta = 0.65 \pm 0.02$ (n=0).

have concluded that the scaling models are correct in predicting rotation curves that are declining more steeply with increasing power-law exponent n (e.g. Efstathiou et al., 1988; Warren et al., 1992). We here propose a different explanation for this observation that for fixed radius, the slope of the rotation curve is steeper in the $n = 0$ simulation than in the n=−1 simulation. From the normalized plots in Fig. 12 we see that in the n=−1 simulation, objects in general have a greater characteristic radius than objects of the same mass in the $n = 0$ simulation. Since clusters in both simulations have density profiles that are excellently fitted by the Hernquist model, their rotation curves should be similar apart from different normalizations. A smaller characteristic radius implies, for the same mass, a steeper profile at the same radius, even when the overall shape of the curves is the same. This observation can therefore not be considered to justify the infall models. One needs to carefully examine the density profiles themselves and these are clearly not power-laws.

These conclusions are corroborated by the results presented in the lower panels of Fig. 15. In that figure the average rotation curves are shown for the clusters in the two simulations. The averaging was performed using the half-mass radius and the mass of the clusters as they were extracted from the simulations, without any model fitting. The figure shows that within the uncertainties the rotation curves are the same for the two simulations, corroborating the conclusions drawn above.

Nevertheless one would expect the initial conditions to show up somewhere, be it in the amplitude of the relation $R \propto M^\beta$ or in the value of the exponent. Our observations are limited to two simulations and clearly it would be very useful to repeat the above analysis for a greater range of initial conditions.
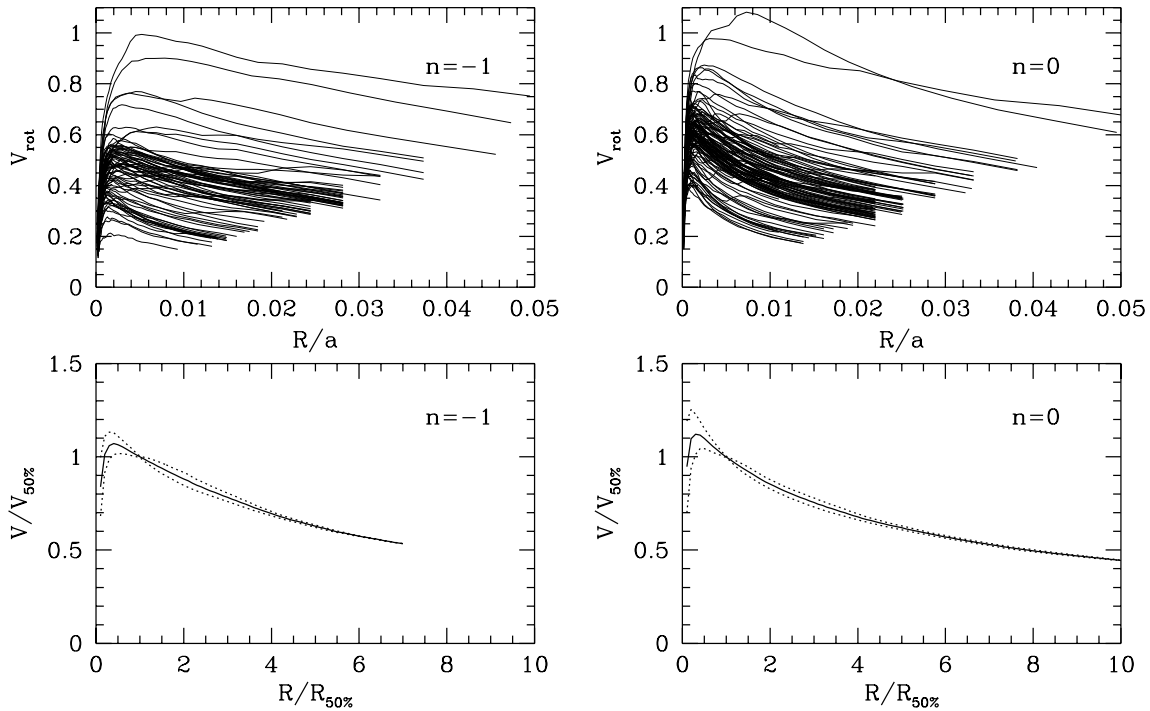
Figure 15: Upper panels show the rotation curves for the clusters from the simulations, derived from the density profiles. Rotation velocity defined by $V_{rot} = (M(R)/R)^{1/2}$. Scales normalized such that scale of simulation volume is a=1 at final time. In the lower panels these rotation curves are normalized by half-mass radius and corresponding velocity and then averaged.

4 Results II: isolated collapse simulations

In this section we present the results of a number of isolated collapse simulations that were performed to check the structural properties of clusters evolved from a greater range of initial conditions. Our main aim was again to determine the density profile of the resulting objects and compare these to the Hernquist and Jaffe models, and also to the more general class of 'η-models' defined above. Depending on the nature of the initial model, we used two different simulation algorithms. In those cases where one expects substructure to develop and relax on timescales short compared to the evolution of the cluster as a whole, we used a version of Hernquist's TREE-code. This code allows one to follow the evolution of clustering with a high spatial resolution over the whole simulation volume. In cases where the predominant evolution was infall onto a central condensation, we used a code originally developed by van Albada (1982), where the potential is expanded in spherical harmonics on a radial grid with highest resolution in the inner parts (SPEXP code). The advantage of this over the TREE code is its speed, the SPEXP algorithm being linearly dependent on the number of particles. Due to the spatial dependence of the force resolution the SPEXP-code is not well suited for following the evolution of small scale structure outside of the inner regions.

We studied four types of initial conditions. The first two classes of models were discussed already in Chapter 4. These models are constructed out of the initial conditions of the
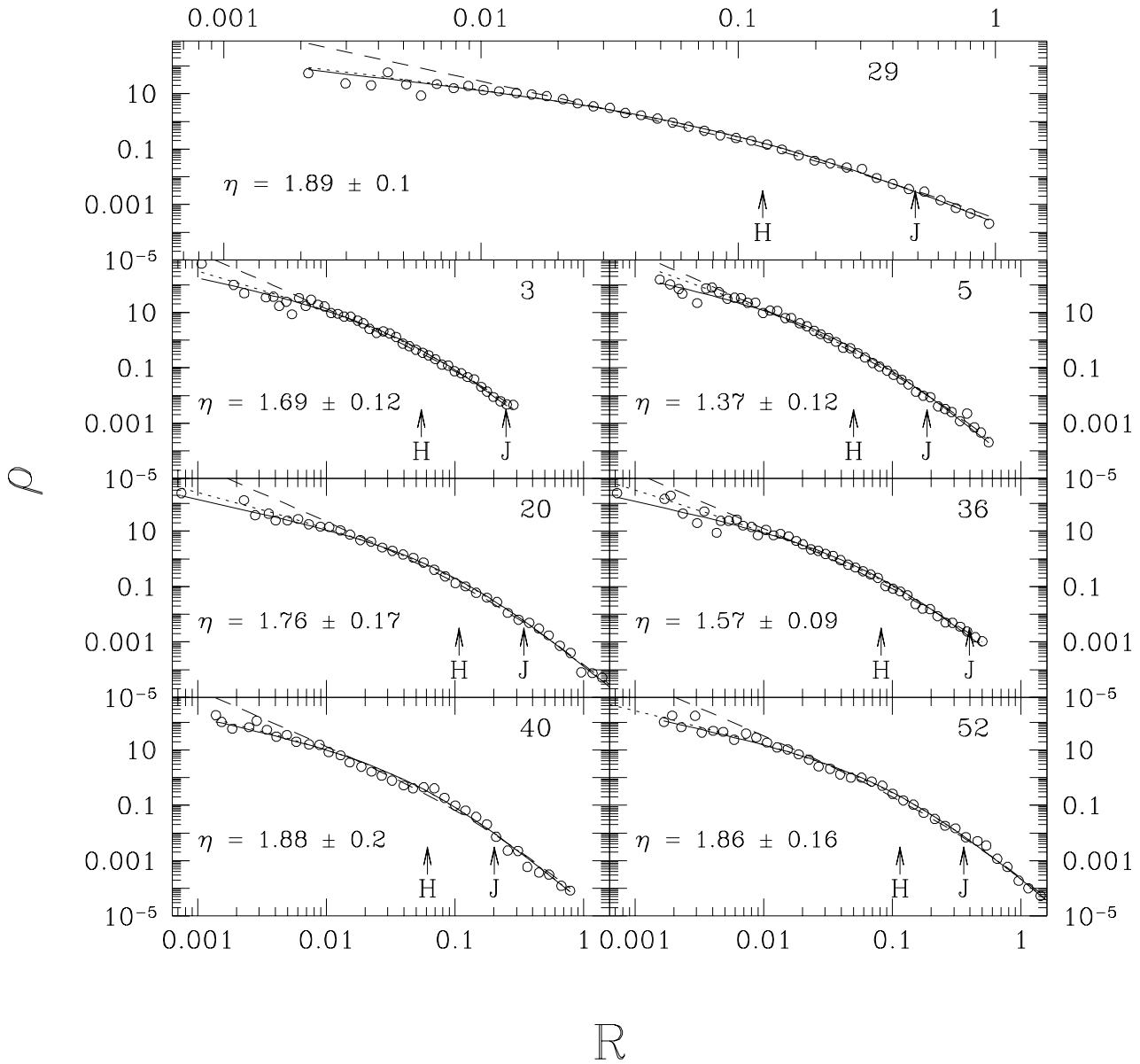
Figure 16: Density profiles for isolated collapse simulations using the TREE-code of clusters extracted from n=−1 cosmological simulation. Curves give best fits to Hernquist model (solid line), Jaffe model (dashed line) and η-model (dotted line). The value for η is indicated, as are the characteristic radii obtained from the two-parameter fits.

n=−1 cosmological simulations. For some of the clusters of the final output time of that simulation, we extracted the corresponding points at the initial time. Around the center of mass of these points a sphere was drawn with a radius of order the maximum distance of the cluster points to the center. The points enclosed by this sphere constituted the final, enlarged cluster, which we then evolved in isolation using the TREE code. From these
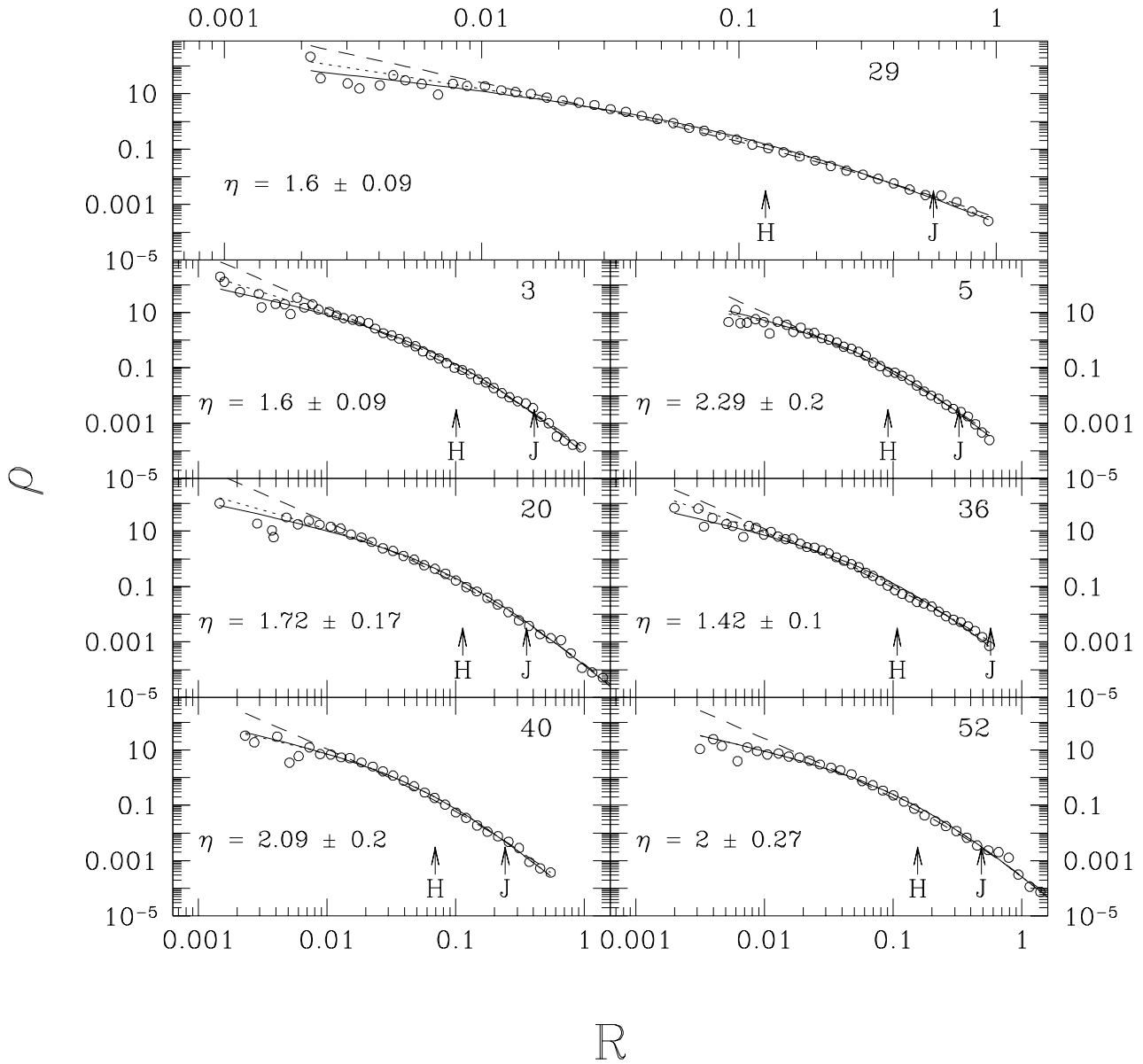
Figure 17: Density profiles for isolated collapse simulations using the SPEXP-code (see text), for spherically symmetrized versions of same clusters as in Fig. 16.

models, a second set of spherically symmetric protoclusters was constructed by angularly randomizing the positions of the points of these cluster around the center of mass, leaving the initial radius and radial velocity of the points constant. This class of models was evolved using the SPEXP code. In Chapter 4 these clusters were used to compare the evolution in isolation with that in the fully cosmological environment. In Figs. 16 and 17 we show the resulting density profiles, determined from the highest density peak of the clusters, together with the best fitting model profiles, both from the Hernquist and Jaffe two-parameter fits,
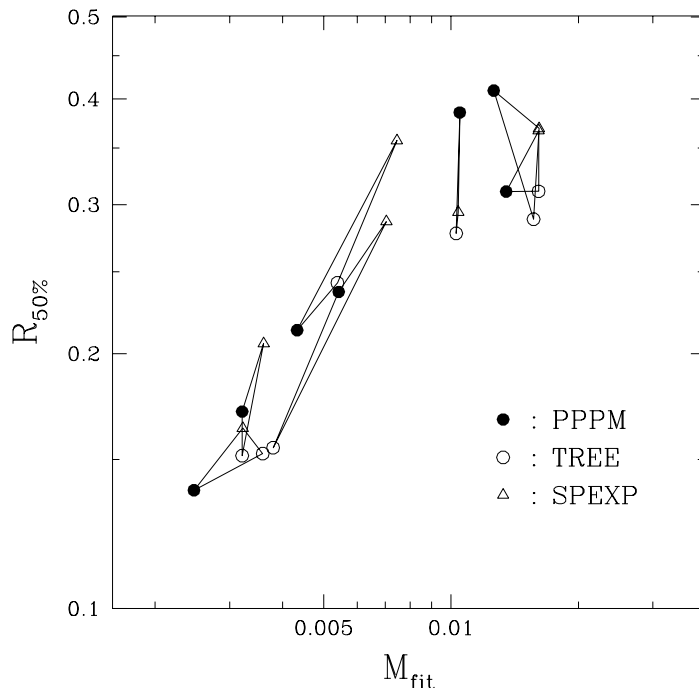
Figure 18: Half-mass radii and total masses from three-parameter fits for the three versions of the clusters in Fig. 16 and 17.

and the η-model three-parameter fits. Clearly, the models fit the end products of these isolated collapses as well as they did for the average clusters in the fully cosmological simulation. The parameters from the three parameter fits for the three different versions of the clusters are compared in Fig. 18. There does not seem to be a systematic effect on the fitted parameters, while the ordering in mass and radius between the clusters is preserved.

The second class of models should closely correspond to the idealized models that are investigated in the semi-analytical self-similar infall models, supposed to describe the collapse of clusters from power-law initial perturbation spectra (Fillmore & Goldreich, 1984; Bertschinger, 1985; Zaroubi & Hoffman, 1993). This correspondence should be perfect for our third class of isolated models. This class consists of spherical clusters that have an exactly power-law radial density perturbation :

$$\rho(r) = \bar{\rho}\left(1 + (r/r_0)^{-\gamma}\right). \tag{5.16}$$

Their initial expansion velocity was a pure Hubble flow, $v(r) = Hr, H^2 = 8\pi G\bar{\rho}/3$, to which was added a velocity perturbation in the linearly growing mode corresponding to the density perturbation interior to the radius. We used three choices for the power-law exponent, $\gamma = 0.5, 1, 1.5$, corresponding to power-spectrum exponents, $n = -2, -1, 0$ respectively.

In Fig. 19 we show the final density profiles for six of theses clusters, two for each choice of γ. These clusters had a uniform component of mass $M = 0.05$, in the same units as the cosmological simulations, and the density perturbation within the maximum radius was
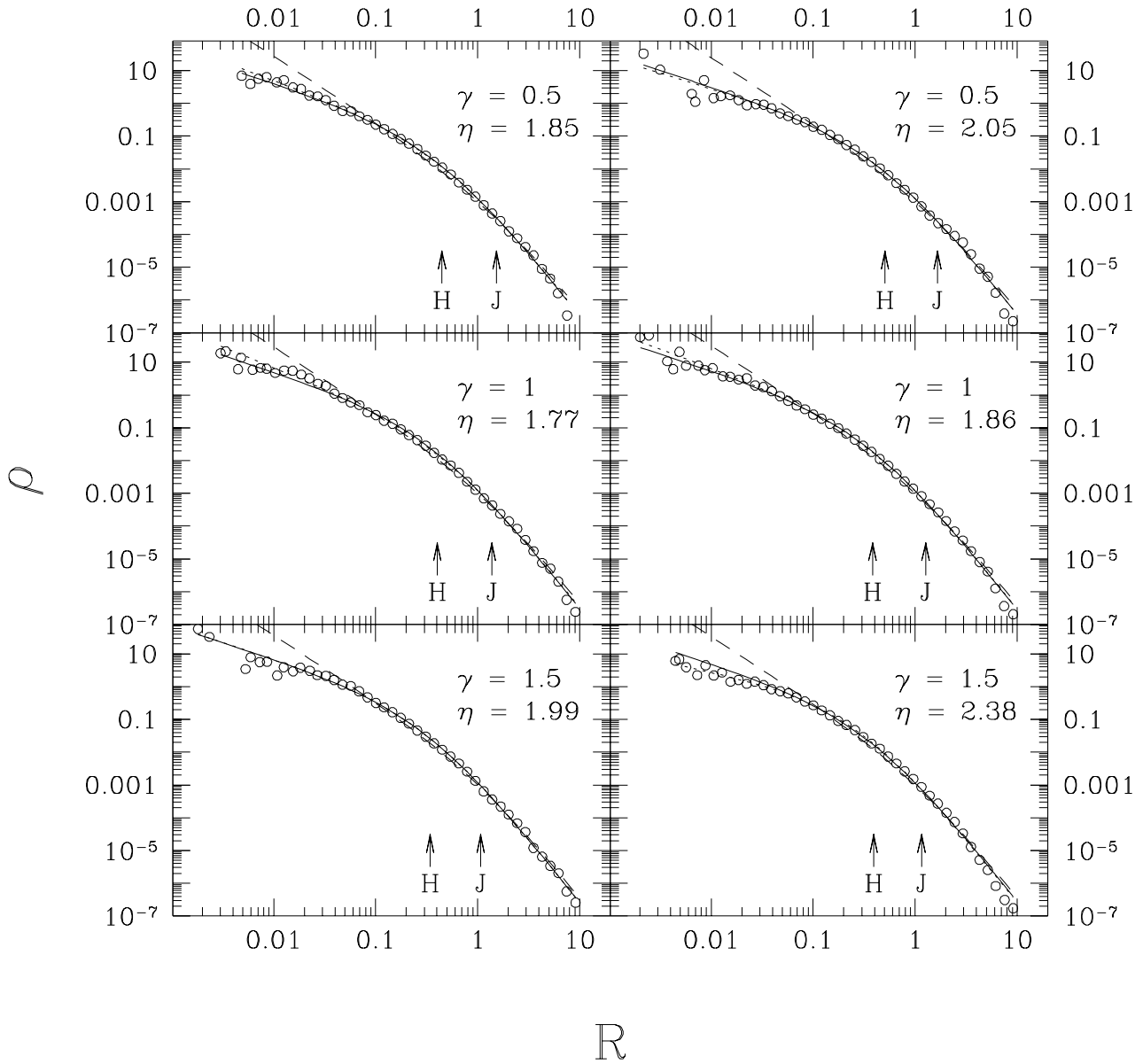
Figure 19: Density profiles for spherical collapse simulations with power-law density perturbation profiles. Power-law exponent γ is indicated, as well as best fit for η from three-parameter fits to η-models. Arrows indicated by H(ernquist) and J(affe) give characteristic scaling radii from two-parameter fits to corresponding models. Lines give best fits for these models as in Fig. 16.

$\delta(r_{max}) = 0.05$. The density profiles are very well fitted by the Hernquist profile and clearly less so by the Jaffe profile, which in this case is significant since the resolution is much higher than the characteristic scales of the clusters. In Fig. 20 we plot the characteristic radii versus γ. There is a clear anti-correlation between the value of γ and the value of $R_{50\%}$, which implies that $R_{50\%}$ increases with decreasing n, just as was suggested in the
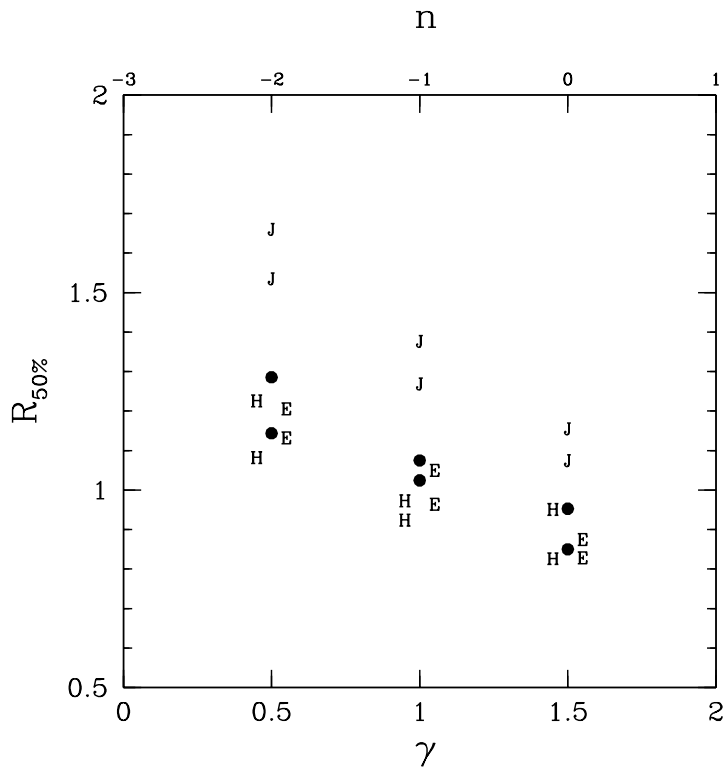
Figure 20: Half-mass radii for the clusters in fir. 19, determined from fits to Jaffe, Hernquist and η-models, as function of power-law exponent γ of initial density perturbation profile.

previous section.

The final set of models is similar to the clumpy models investigated by van Albada (1982). Spherical, uniform groups of points were uniformly distributed over a spherical region. Both the points within each group and the groups as a whole were given random velocities that were a fraction of the virial velocity of the whole cluster. The clusters were *not* expanding. For certain choices of the parameters, these models were shown by van Albada to lead to final surface density profiles that were very well fitted by a de Vaucouleurs profile (van Albada, 1982). The radial density profiles of the clusters simulated here are shown in Fig. 21. The different clusters correspond to various choices for the radius of the sub-clusters, the random velocities of the sub-clusters and of the particles within each sub-cluster. The correspondence with the model profiles is not very good for these clusters. In all cases the inner regions are too flat for both the Jaffe and the Hernquist models, while the outer regions are too steep. The η-model fits are badly constrained and give unphysical values, $\eta > 3$. The formation of a flat, core-like region, which was also observed by van Albada in his models, may be due to the constraint that the course-grained phase space density can not increase to values higher than the initial maximum fine-grained phase space density (e.g. Carlberg, 1986). As Carlberg et al. (1986) show, in such cases dissipation may help to achieve higher core densities.
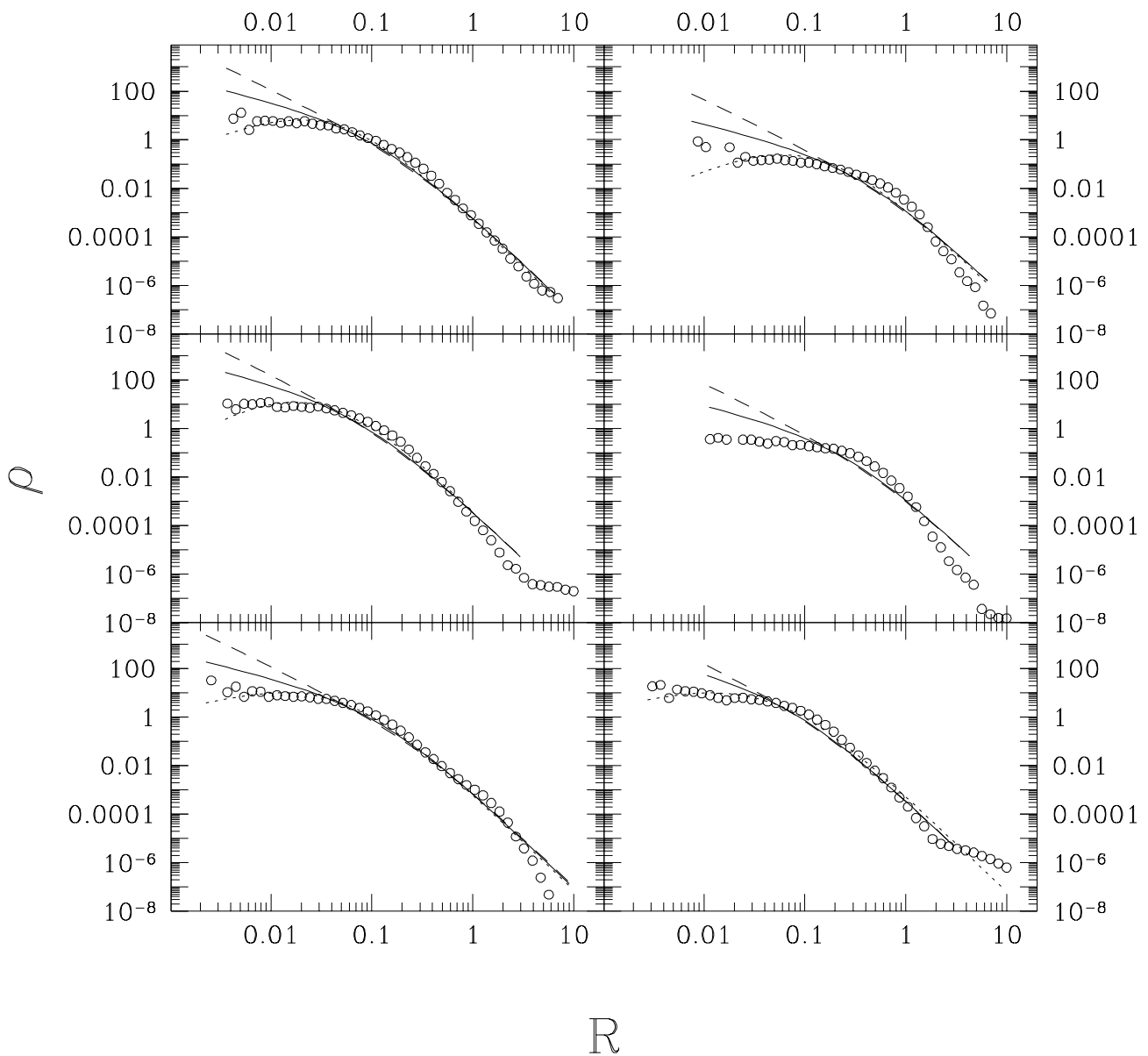
Figure 21: Density profiles from clumpy collapse simulations using the SPEXP-code. Lines correspond to model fits as in Fig. 16.

5 Summary and discussion

In this chapter, the question has been addressed of what may be the outcome of purely gravitational collapse processes. We have done so by analyzing the radial density profiles of clusters that were formed in dissipationless collapse simulations. Our main aim was to try to resolve the apparent discrepancy between the two main pictures of the approach to equilibrium, namely violent relaxation (Lynden-Bell, 1967) and secondary infall (Fillmore &

Goldreich, 1984; Bertschinger, 1985). These processes give rise to different types of objects, both of which have apparently been observed and reproduced in N-body simulations.

Observations show that rotation curves of spiral galaxies are flat out to large radii, while the surface density profiles of elliptical galaxies are well described by a de Vaucouleurs, $R^{1/4}$profile. The first observation is explained by assuming that the density profile of the underlying dark halo asymptotically behaves as $\rho \sim R^{-2}$, while the de Vaucouleurs profile is well reproduced by the so-called Hernquist profile, which behaves asymptotically as $\rho \sim R^{-4}$. Dark halos are usually equipped with flat cores, $\rho \sim$ constant for R small, while the Hernquist model diverges for $R^{-1}, R \to 0$. According to Sanders & Begeman (1994), this last characteristic of the Hernquist profile actually would make it an ideal model also for the dark halos of spiral galaxies, since this behaviour might reproduce the successes and implied correlations from MOND fits to observed rotation curves (Begeman et al., 1991). Indeed, Sanders & Begeman (1994) were able to fit several rotation curves very well using essentially one parameter Hernquist models, where the total mass and characteristic radii were coupled as $R_H \propto M_H^{1/2}$. If dark halos actually have a Hernquist profile and if the mass and radius are related as above, this might explain the success of the MOND fits, without requiring new gravitational physics, and, moreover, would provide an explanation for the Tully-Fisher relation. If indeed dark-halos can be described by the same models as elliptical galaxies, this would strengthen the belief that these objects have originated from similar collapse processes.

On the theoretical side, both forms of the density profile in dark halos have been explained using dissipationless collapse processes. Power-law halos result from semi-analytical self-similar infall calculations where $\rho \sim r^{-2}$ is achieved for the correct choice of initial conditions (Fillmore & Goldreich, 1984; Bertschinger, 1985; Zaroubi & Hoffman, 1993). These results have found support in various cosmological N-body simulations, in which it was found that rotation curves are flatter for (power-law) initial conditions, $P(k) \propto k^n$, with lower values for n (e.g. Efstathiou et al., 1988; Warren et al., 1992; Crone et al., 1994). On the other hand, collapse simulations from clumpy initial conditions, have reproduced the de Vaucouleurs profile of elliptical galaxies (van Albada, 1982), while high resolution collapse simulations from CDM initial conditions with an approximate inclusion of the external universe produced clusters whose density profiles were described by the Hernquist model to high precision (Dubinski & Carlberg, 1991).

In this paper we have shown that indeed the Hernquist and to a lesser extent also the Jaffe models, provide an accurate description of the radial density profiles of clusters that were evolved from a range of scale-free initial conditions. This means that the scale-free nature of the initial conditions is broken during the gravitational evolution of the individual clusters. At the same time it was shown that the basic model parameters, namely the mass and the characteristic scale, are strongly correlated:

$$R_c = A(n)M_c^{\beta(n)}. \tag{5.17}$$

Here we propose that, instead of working on the individual cluster level, as is assumed in the infall models for cluster formation, the initial conditions determine the quantitative properties of this scaling relation. In this picture, the non-power-law shape of the individual cluster profiles is determined by collective, violent, relaxation processes, in which the initial

conditions are remembered only in so far as they determine the form of the above scaling relation. As the artificial cold and clumpy collapses show, the functional form of the final density profile may at least to some level be determined by the initial conditions as well, but for the range of more realistic initial conditions investigated in this work and in the work of other authors, it seems that the η-models in general, and the Hernquist model in particular, form a more or less universal class of model profiles to which the clusters evolve in their final relaxation stages.

One consequence of this is that the flatness of rotation curves of spiral galaxies is not necessarily a consequence of the initial conditions. In the past, rotation curves were derived for clusters in cosmological simulations, which appeared flatter for lower values of the exponent n in the power-spectrum $P(k) \propto k^n$ (e.g. Efstathiou et al., 1988). Simple analytical arguments predict flat rotation curves for n=−2, which happens to be the logarithmic slope of the Cold Dark Matter (CDM) spectrum at galaxy scales. These same arguments do however predict power-law density profiles, which are not observed in the simulations investigated here.

As shown by Sanders & Begeman (1994), dark halos with a Hernquist density profile can explain the rotation curves around spiral galaxies. To compare their results to the present ones we need to assign physical sizes to the simulated clusters. Since the simulations are essentially scale free, there is no unique way in which such an identification may be obtained (see Barnes & Efstathiou, 1987, for a discussion of several methods). Here we are interested in comparing the correlation between mass to a radius to the observed relation. We will therefore assume that the final output corresponds to the present time. We will first assume that a cluster of 10000 points corresponds to a mass of $10^{12} M_\odot$; the total mass in the simulations was therefore $10^{14} M_\odot$. Writing the Hubble parameter at present as $H_0 = 100h$ km/s, we obtain for the density in the present Universe $\rho_c = 3H_0^2/8\pi G = 2.78 \times 10^{11} h^2 (M_\odot/Mpc^3)$. We may now calculate the size of the simulating box, which is $L = 7.1h^{-2/3}$ Mpc. From Fig. 12 we see that a mass of $10^{12} M_\odot$ in the n=−1 simulation corresponds to a radius of roughly $R_0 = 0.0055 * 7.1h^{-2/3} \approx 39h^{-2/3} kpc$. For the n=0 simulation the radius is $R_0 = 27kpc$. The results obtained by Sanders & Begeman (1994) indicate that a mass of $10^{12} M_\odot$ corresponds to a radius of $R_0 = 123kpc$. They took a value of $H_0 = 75km/s/Mpc$ for the Hubble constant, which then gives $R_0 = 47kpc$ and $R_0 = 33kpc$ for n=−1 and n=0 respectively. These values fall short of the observed values, but one might expect such a result. The CDM spectrum has a logarithmic slope corresponding to an n=−2 power-law spectrum at galaxy scales. For n=−2 we expect the characteristic radius to be still larger, which may resolve this mismatch.

There is a worse problem with this normalization however. The implied correlation length, the radius at which the two-point correlation function reaches unity, would be $r_0 \approx 0.5Mpc$ (for n=−1), an order of magnitude smaller than is observed in the Universe (see Chapter 1). One may normalize the simulations such that these values agree, but it turns out that the implied characteristic radii are then even smaller than with the previous normalization.

Some interesting questions still await an answer. First, the shape of the dark halos around spiral galaxies is still badly constrained. The present work indicates that halos are essentially finite. This may be an artifact of the limited range of initial conditions that

has been probed. On galactic scales, the power spectrum is expected to have a power-law exponent $n \sim -2$ in the context of the CDM model. It may well be that halos would overlap before reaching the asymptotic $\rho \sim r^{-4}$ behaviour. In such cases both violent relaxation and secondary infall may only offer a limited description of the true formation process. Also, some claims have been made that dwarf galaxies do not conform to a picture with singular dark halos (Moore, 1994; Flores & Primack, 1993).

Second, in the present work we claim that the self-similar infall calculations do not correctly describe the evolution of overdensities after turn-around. Apparently the extra degrees of freedom in the actual three-dimensional collapse process are not adequately described by the purely radial infall approximation. Instead, violent relaxation seems to be at work at some level in cosmological environments just as earlier it was shown to act in isolated collapses from clumpy initial conditions (van Albada, 1982). It would clearly be desirable to obtain an analytical treatment of this relaxation process and thus understand how the $R^{1/4}$–profiles are generated on a more fundamental level than N-body simulations may ever provide. Some attempts have been made in that direction, but none have been totally convincing (Bertin & Stiavelli, 1984; May & van Albada, 1984; Stiavelli & Bertin, 1987; Hjorth & Madsen, 1991, 1993).

Third, it is interesting to investigate the importance of these results for galaxy formation theories. There it is usually assumed that galaxies form within an isothermal dark halo. It is very likely that the actual shape of the halo, together with the various correlation of its properties, will influence the properties of the final galaxy. The observed scaling between mass and radius can easily be translated into a Tully-Fisher relation, except for the fact that the scatter in halo properties already seems larger than the observed scatter (see also Eisenstein & Loeb 1995). Understanding this relation would of course be very desirable as well. To assess this problem one must clearly also know how these properties depend on the initial conditions. Especially interesting would be to see whether these scaling relations hold when the initial conditions are not scale-free, such as is the case for the cold dark matter model.

References

Baldwin, J.E., Lynden-Bell, D., Sancisi, R., 1980, MNRAS, 193, 313

Barnes, J., Efstathiou, G., 1987, ApJ, 319, 575

Begeman, K.G., Broeils, A.H., Sanders, R.H., 1991, MNRAS, 249, 523

Bertschinger, E., 1985, ApJS, 58, 39

Bertin, G., Stiavelli, M., 1984, A&A, 137, 26

Carlberg, R.G., 1986, ApJ, 310, L1

Carlberg, R.G., Lake, G., Norman, C.A., 1986, ApJ, 300, L1

Crone, M.M., Evrard, A.E., Richstone, D.O., 1994, ApJ, 434, 402

Dehnen, W., 1993, MNRAS, 265, 250

de Vaucouleurs, G., 1948, Ann.d'Ap., 11, 247

Dubinski, J., Carlberg, R.G., 1991, ApJ, 378, 495

Eadie et al., 1971, Statistical methods in experimental physics, North Holland

Efstathiou, G., Davis, M., Frenk, C.S., White, S.D.M., 1985, ApJS, 57, 241

Efstathiou, G., Frenk, C.S., White, S.D.M., Davis, M., 1988, MNRAS, 235, 715

Eisenstein, D.J., Loeb, A., 1995, preprint astro-ph/9506074

Fillmore, J.A., Goldreich, P., 1984, ApJ, 281, 1

Fish, R.A., 1964, ApJ, 139, 284

Flores, R.A., Primack, J.R., 1993, Santa Cruz preprint SCIPP 93/01

Gott, J.R., Rees, M.J., 1975, A&A, 45, 365

Gunn, J.E., 1977, ApJ, 218, 592

Gunn, J.E., Gott, J.R., 1972, ApJ, 176, 1

Hernquist, L., 1990, ApJ, 356, 359

Hjorth, J., Madsen, J., 1991, MNRAS, 253, 703

Hjorth, J., Madsen, J., 1993, MNRAS, 265, 237

Hockney, R. W., Eastwood, J. W., 1982, Computer Simulations Using Particles,
    McGraw Hill, New York

Hoffman, Y., 1988, ApJ, 328, 489

Hoffman, Y., Shaham, J., 1985, ApJ, 297, 16

Jaffe, W., 1983, MNRAS, 202, 995

Kaastra, J.S., van Bueren, H.G., 1981, A&A, 99, 7

Katz, N., 1991, ApJ, 368, 325

Kormendy J., 1982, in Morphology and Dynamics of Galaxies, 12th Advanced Course,
    Swiss Society of Astronomy and Astrophysics, Saas-Fee

Lynden-Bell, D., 1967, MNRAS, 136, 101

May, A., van Albada, T.S., 1984, MNRAS, 209, 15

Moore, B., 1994, Nat, 370, 629

Press, W.H., Flannery, B.P., Teukolsky, S.A., Vetterling, W.T., 1989, Numerical Recipes,
    Cambridge University Press, Cambridge

Quinn, P.J., Salmon, J.K., Zurek, W.H., 1986, Nat, 322, 329

Rix, H.-W., Zaritski, D., 1995, ApJ, 447, 82

Richter, O.-G., Sancisi, R., 1994, A&A, 290, L9

Sanders, R.H., 1990, A&AR, 2, 1

Sanders, R.H., Begeman, K.G., 1994, MNRAS, 266, 360

Sarazin, C.L., 1980, ApJ 236,75

Sarazin, C.L., 1988, X-ray Emission from Clusters of Galaxies, Cambridge University Press,
    Cambridge

Schombert, J.M., 1986, ApJS, 60, 603

Stiavelli, M., Bertin, G., 1987, MNRAS, 229, 61

Tremaine, S. et al., 1993, AJ, 107, 634

van Albada, T.S., 1982, MNRAS, 201, 939

van Albada, T.S., Bahcall, J.N., Begeman, K.G., Sancisi, R., 1985, ApJ, 295, 305

Warren, M.S., Quinn, P.J., Salmon, J.K., Zurek, W.H., 1992, ApJ, 399, 405

West, M.J., Dekel, A., Oemler, A., 1987, ApJ, 316, 1

West, M.J., Oemler, A., Dekel, A., 1989, ApJ, 346, 539

White, S.D.M., Rees, M.J., 1978, MNRAS, 183, 341

White, S.D.M., 1993, Formation and Evolution of Galaxies, Les Houches lectures, preprint

Young, P.J., 1976, AJ, 81, 807

Zaroubi, S., Hoffman, Y., 1993, ApJ, 416, 410